Wnt-Ror-Dvl signalling and the dystrophin complex organize planar-polarized membrane compartments in *C. elegans* muscles

Alice Peysson[1, #], Noura Zariohi[1, #], Marie Gendrel[2], Amandine Chambert-Loir[1], Noémie Frébault[1], Elise Cheynet[1], Olga Andrini[1], Thomas Boulin[1,*]

[1] Université Claude Bernard Lyon 1, CNRS UMR 5284, INSERM U1314, MeLiS, Lyon 69008, France
[2] Institut de Biologie de l'Ecole Normale Supérieure (IBENS), Ecole Normale Supérieure, CNRS, INSERM, Université Paris Sciences et Lettres Research University, Paris 75005, France
[#] These authors contributed equally
* Corresponding author

6 Figures, 7 Supplementary Figures, 1 Supplementary Table

Keywords: Wnt signalling, planar cell polarity, *C. elegans*, ion channels, dystrophin-associated protein complex, plasma membrane compartmentalization

ABSTRACT

Cell polarity mechanisms allow the formation of specialized membrane domains with unique protein compositions, signalling properties, and functional characteristics. By analysing the localization of potassium channels and proteins belonging to the dystrophin-associated protein complex, we reveal the existence of distinct planar-polarized membrane compartments at the surface of *C. elegans* muscle cells. We find that muscle polarity is controlled by a non-canonical Wnt signalling cascade involving the ligand EGL-20/Wnt, the receptor CAM-1/Ror, and the intracellular effector DSH-1/Dishevelled. Interestingly, classical planar cell polarity proteins are not required for this process. Using time-resolved protein degradation, we demonstrate that –while it is essentially in place by the end of embryogenesis– muscle polarity is a dynamic state, requiring continued presence of DSH-1 throughout post-embryonic life. Our results reveal the unsuspected complexity of the *C. elegans* muscle membrane and establish a novel genetically tractable model system to study cellular polarity and membrane compartmentalization *in vivo*.

INTRODUCTION

Cell polarization is a fundamental process that organizes distinct subcellular domains within cells. The elaboration of polarized membrane sub-compartments allows these specialized regions to have unique protein compositions, signalling properties, and functional characteristics. Cellular compartmentalization mechanisms rely on a multitude of molecular pathways that engage the cytoskeleton, scaffolding proteins and signalling molecules. Within small cellular ensembles and larger tissues, cell-cell communication and external cues from secreted factors play a major role in regulating cell and tissue polarity.

Wnts are a class of secreted glycoproteins that play a pivotal role in cell polarity by transducing their signals through a variety of pathways. These Wnt pathways are conserved and critical in all metazoans. There are two main classes of Wnt signalling pathways: the canonical Wnt/β-catenin cascade[1] and several β-catenin-independent, so-called non-canonical signalling pathways. Among these non-canonical pathways, the Wnt-Planar Cell Polarity (PCP) module plays a major role in organizing cells in the plane of a tissue. Indeed, PCP is important for many developmental processes regulating the formation of tissues and organs in animals. For instance, PCP proteins regulate the orientation of hair follicles and sensory cells, the shape and movement of cells during gastrulation (e.g., convergent-extension processes) and neural tube closure, or the positioning of cell extensions, such as cilia and axons[2–6].

These non-canonical Wnt signalling pathways are also conserved in the nematode *Caenorhabditis elegans*[7–11]. They have been shown to control directional polarity processes, including convergent extension movements during gastrulation[12], migration of neuronal precursors[13,14], and the extension, guidance, and branching of neuronal projections[15–18]. Generally, antero-posterior (A-P) polarity decisions rely on short and long-range Wnt ligand gradients, which have been visualized *in vivo*[19,20]. In the early worm embryo, short-range signals between contacting cells provide positional instructive cues that direct polarized cell division by orienting the mitotic spindle[21]. Post-embryonically, Wnt signalling has been shown to control asymmetric cell divisions of epithelial seam cells and vulva precursor cells[9,22].

While PCP proteins have been shown to accumulate asymmetrically in some cases[12,23], molecular bridges formed by transmembrane proteins interacting in trans – a hallmark of PCP machineries in flies [3,24] – have however not been observed in *C. elegans*. PCP proteins, instead, act on an individual cell basis, and antero-posterior polarity decisions rely on transient directional cues provided by PCP proteins and/or Wnt ligands[8,9,25]. Thus, despite the strong molecular conservation of Wnt signalling pathways, there is currently no clear example of planar cell polarity at the level of an entire tissue in *C. elegans*.

The musculature of *C. elegans* is organized into two ventral and two dorsal quadrants that run along the length of the body. Each quadrant comprises two bands of successive muscle cells[26]. These muscle cells and their sarcomeres attach to the epidermis through integrin-containing adhesive complexes, forming a network that covers the outer surface of the muscle cells. Additionally, the Dystrophin-Associated Protein Complex (DAPC) connects the intracellular actin cytoskeleton to the extracellular matrix along the muscle sarcolemma[26]. When viewed dorsally and ventrally, body wall muscles appear as diamond-shaped cells (Figure 1A). They project membrane extensions, called “muscle arms”, towards the neurites of presynaptic motoneurons, establishing post-synaptic domains that concentrate ligand-gated ion channels at chemical synapses. The molecular mechanisms that underlie the construction of these membrane nanodomains have been extensively characterized [27]. In comparison, little is known about how membrane proteins are sorted to other parts of the muscle cell and

whether they could be organized into distinct submembrane compartments. In fact, recent transcriptomic analyses have revealed that a surprisingly large number of ion channel genes are co-expressed in *C. elegans* muscle cells, raising interesting questions about their temporal dynamics, individual functions, and subcellular distribution[28–37].

In this study, we reveal the highly structured and polarized organization of the plasma membrane of *C. elegans* body wall muscle cells. By investigating the subcellular localization of ion channels and components of the dystrophin-associated protein complex, we demonstrate that these proteins localize to distinct and remarkably consistent asymmetric membrane compartments. Specifically, the potassium channels TWK-28, TWK-24, and SLO-1 occupy separate but partially overlapping polarized domains located at the tip, center, and posterior region of each muscle cell, respectively. DAPC proteins define further polarity patterns that differ in the anterior and the posterior of each muscle cell. The repetition of these asymmetric membrane compartments along the length of the body bears a striking resemblance to planar polarity patterns observed in other animals. However, we find that conserved PCP proteins are not required for this process. Through a candidate gene approach, we have found that muscle polarity relies on the Wnt ligand EGL-20, the Wnt receptor CAM-1/Ror, and the intracellular effector DSH-1/Dishevelled. Remarkably, DSH-1 is continuously required to maintain muscle polarity, and its post-embryonic re-expression can restore defective cell polarity, highlighting the dynamic nature of muscle polarity. Taken together, these findings uncover the intricate organization of the worm's sarcolemma and reveal a new instance of planar cell polarity in *C. elegans*.

RESULTS

Ion channel localization reveals a remarkably complex and planar-polarized organization of the muscle sarcolemma

Potassium-selective channels are the largest family of ion channels in the *C. elegans* genome. Transcriptomic data indicate that up to 21 distinct potassium channel subunits are co-expressed in body wall muscle cells[28,34]. Yet, little is known about the subcellular localization of most of these channels. To address this question, we used two previously published reporter strains (TWK-18[32]; SLO-1[33]) and engineered knockin lines for six two-pore domain (K2P) channels (TWK-8, TWK-12, TWK-24, TWK-28, TWK-42, TWK-43) using CRISPR/*Cas9*-based gene editing.

Careful analysis of these fluorescent reporters revealed a remarkable diversity of situations. While TWK-8 was present throughout the cell surface (Figure S1A), TWK-12 and TWK-43 were only visible in muscle arms and on the lateral sides of body wall muscle cells, but not on the outer surface that faces the hypodermis (Figure S1B). Conversely, TWK-18 and TWK-42 showed distinct distribution patterns on the outer face of each muscle cell, which were either broad (TWK-18) or punctate (TWK-42) (Figure S1A).

The localization of SLO-1, TWK-24 and TWK-28 were the most striking (Figures 1A and 1B). Indeed, TWK-28 was concentrated at the anterior tip of each muscle cell, in a singular comet-shaped pattern. Conversely, SLO-1 channels was absent from the anterior part of the cell and formed a regularly-spaced punctate pattern in the centre and posterior region. Finally, while TWK-24 channels appeared to be broadly distributed at first glance, outlining muscle cells revealed that TWK-24 was in fact absent from their extremities and enriched in the central portion of the cell.

Given that SLO-1, TWK-24, and TWK-28 domains partially overlap at the scale of a muscle cell, we wondered whether they were also colocalized in membrane nanodomains. By

simultaneously labelling the three channels, we observed that individual ion channel clusters were clearly separable using diffraction-limited confocal microscopy, suggesting that they could be part of distinct protein complexes, even where their distribution patterns overlap at the cellular scale (Figure 1C).

The SLO-1 channel has been shown to physically interact with the integral membrane protein ISLO-1[38]. Therefore, we generated a fluorescent knockin line to assess its subcellular localization. Remarkably, ISLO-1 and SLO-1 did not show identical distribution patterns. While ISLO-1 colocalized with SLO-1 in the posterior part of the cell (Figure 1D), ISLO-1 was also clearly enriched at the anterior tip in a comet-shaped pattern that coincided perfectly with TWK-28 (Figure 1E). Hence, the distribution pattern of ISLO-1 defines a fourth class of asymmetrical subcellular localization with both anterior and posterior domains, in which ISLO-1 is organized in very different subcellular patterns depending on its position in the cell, i.e., a comet-shaped anterior pattern, and a punctate, regularly-spaced, posterior pattern.

Taken together these observations reveal the remarkably complex molecular makeup of the plasma membrane of *C. elegans* muscle cells. They demonstrate, for the first time, the existence of asymmetric membrane compartments with distinct molecular compositions. Furthermore, as these asymmetric distribution patterns are repeated in each muscle cells all along the length of the worm, they also constitute the first examples of planar cell polarity at the tissue scale in *C. elegans*.

Dystrophin and dystrophin-associated proteins are required for TWK-28 surface expression

To try to understand how the TWK-28 potassium channel is asymmetrically localized in muscle cells, we performed a forward genetic screen based on the rationale that the disruption of factors required to address TWK-28 to the cell surface would suppress the effect of a hyperactivating gain-of-function mutation. We previously demonstrated that the activity of vertebrate and invertebrate two-pore domain potassium channels can be tuned by mutating a key residue in the second transmembrane domain, named TM2.6[39]. After confirming that this mutation increased TWK-28 activity using heterologous expression in *Xenopus* oocytes (Figure S1C), we used CRISPR/*Cas9* gene editing to build a *twk-28* TM2.6 gain-of-function mutant (*bln485*, TWK-28 L210T). These mutants displayed strongly reduced locomotion, as expected for a gain-of-function mutation that decreases the excitability of muscle cells (Figure S1D).

After screening approx. 15.000 mutagenized haploid genomes, we obtained 182 independent suppressor lines that had regained near wild-type mobility. Among these, 102 were extragenic revertants based on genetic segregation, i.e., mutants that did not alter the *twk-28* gene sequence. Using whole genome resequencing, we analysed 25 of these mutants and found that 14 were loss-of-function alleles of *dys-1,* the *C. elegans* ortholog of dystrophin, and that one was an allele of *islo-1* (Figure S1E).

To measure their impact on TWK-28 surface expression, we combined *dys-1* and *islo-1* mutants with the fluorescently-labeled TWK-28 reporter (Figures 2A and 2B). We observed a drastic change in *dys-1(bln582)* and *islo-1(bln549)* mutants as TWK-28 fluorescence was reduced by 74% and 70% relative to wild type, respectively. Interestingly, *dys-1(bln582)* harbours an early stop codon at W110. This mutation affects only the longest dystrophin isoform that contains both calponin-homology actin-binding domains. To verify whether the remaining TWK-28 fluorescence could be due to residual activity of shorter dystrophin isoforms, we generated *syb2174*, a molecular null allele that deletes the entire 31 kb-long *dys-*

200 *1* genomic locus. This allele showed the same effect as *bln582*, arguing that the W110Stop
201 mutation is a functional null allele for TWK-28 localization (Figure 2A).
202 In addition to dystrophin, *C. elegans* muscle express the orthologs of the dystrophin-
203 associated proteins dystrobrevin (*dyb-1*), syntrophin (*stn-1*, *stn-2*), and sarcoglycan/Sgc (*sgca-*
204 *1*, *sgcb-1*, *sgn-1*) (see below and Supplementary Table S6). We therefore tested the
205 requirement of these DAPC proteins for TWK-28 localization using loss-of-function mutants.
206 Individual sarcoglycan mutants and a triple knock-out did not modify TWK-28 fluorescence
207 levels (Figures S1F and S1G). In contrast, *dyb-1(cx36), stn-1(ok292)* and *stn-2(ok2417)* each
208 significantly reduced TWK-28 fluorescence, by approx. 55%, 37%, and 76%, respectively,
209 suggesting a predominant requirement of STN-2 (Figures 2B and 2D). Importantly, in all cases,
210 residual TWK-28 channels were still restricted to the anterior tip of muscle cells, indicating that
211 targeting of TWK-28 to the comet-shaped domain is not solely dependent on DAPC proteins.
212 To assess whether dystrophin was more broadly required for the localization of muscle-
213 expressed K2P channels, we combined four fluorescent knockin lines with a *dys-1* loss-of-
214 function allele. We observed no obvious impact for any of these channels, whether they were
215 uniformly distributed (TWK-8, TWK-18, TWK-42), or asymmetrically localized (TWK-24)
216 (Figure S1A).
217 Taken together, these results suggested a model in which TWK-28 could be stabilized
218 at the sarcolemma via interactions with the DAPC, as is the case for voltage-gated sodium
219 channels and inwardly-rectifying potassium channels in vertebrate cardiomyocytes [40,41].
220 Indeed, a short amino acid sequence in the cytoplasmic C-terminus of $Na_V1.5$ and Kir4.1 is
221 recognized by the PDZ domain of syntrophin, which itself binds to dystrophin and thus
222 stabilizes these ion channels at the plasma membrane. Using *in silico* prediction algorithms [42],
223 we identified a putative PDZ-binding sequence in the carboxy-terminus of TWK-28 (Figure 2C).
224 After inserting a premature stop codon that removed these amino acids by gene editing (Figure
225 2C) in the context of the mNeonGreen-tagged TWK-28 fluorescent reporter strain, we
226 observed a dramatic reduction in the number of TWK-28 channels (approx. 80%) at the cell
227 surface, similar to *dys-1* and *stn-2* mutants (Figures 2D and 2E). Combining this truncated
228 TWK-28 channel with a molecular null allele of *dys-1* did not further reduce TWK-28-associated
229 fluorescence (Figure 2E), which is consistent with a model in which TWK-28 is recognized by
230 syntrophins and stabilized at the plasma membrane by the dystrophin-associated protein
231 complex.
232
233 **TWK-28 dynamics following post-embryonic DYS-1 degradation and recovery**
234 To examine the dynamics of the relationship between TWK-28 and the DAPC, we developed
235 a temporally-controlled dystrophin degradation strategy using the auxin-inducible degron (AID)
236 system[43]. To monitor DYS-1 levels and subcellular localization, we associated an
237 mNeonGreen coding sequence with the AID degron sequence. This knockin line was fully
238 functional as we did not observe *dys-1* loss-of-function phenotypes (e.g., exaggerated head
239 bending, reduction in TWK-28 surface expression).
240 Confocal imaging revealed a broad distribution of DYS-1 on the outer face of muscle
241 cells, facing the epidermis (Figure 2G). Consistent with the model that TWK-28 is recruited to
242 the DAPC, DYS-1 and TWK-28 were well colocalized in the anterior tip of each muscle cell
243 (Figure 2H). Hence, while dystrophin is broadly distributed throughout the sarcolemma, it is
244 also enriched at the tip of muscle cells.
245 We first tested whether DYS-1 could be degraded by observing the offspring of
246 hermaphrodites grown on auxin (Figures 2F and 2G). Although a very small fraction of the
247 dystrophin-associated fluorescence remained detectable, it was drastically diminished in these

248 auxin-treated worms (Figures 2G and 2H). Consistently, worms exposed to auxin throughout
249 their life displayed the exaggerated head-bending phenotype observed in dystrophin null
250 mutants, confirming effective dystrophin degradation. Moreover, the impact of DYS-1
251 degradation was comparable to *dys-1* null mutants (Figure 2A), since TWK-28 fluorescence
252 was reduced by 73% compared to untreated animals (Figures 2H and 2J).
253 Using this assay, we could analyse the kinetics of dystrophin recovery over 24 hours,
254 starting at the L4 larval stage (Figure 2F). After removing animals from auxin-supplemented
255 media, we saw a partial restoration of DYS-1-mNeonGreen fluorescence throughout the
256 muscle cell and at the anterior tip. wrmScarlet-tagged TWK-28 channels also recovered
257 notably over the 24-hour time period, but did not fully reach wild-type levels (Figures 2I and
258 2J). Notably, TWK-28 puncta were associated with DYS-1, in line with a direct association of
259 TWK-28 with the DAPC (Figure 2I). These data indicate that dystrophin complexes can be
260 partially reassembled post-embryonically.
261
262 **Dystrophin-associated proteins localize to asymmetric membrane compartments**
263 Given the polarized enrichment of dystrophin at the anterior tip of muscle cells, we used
264 CRISPR/*Cas9* gene editing to label all members of the worm's DAPC complex[44] and
265 characterized their subcellular distribution.
266 In vertebrates, dystroglycan is a central component of the DAPC, linking the
267 extracellular matrix to the intracellular cytoskeleton via dystrophin. In *C. elegans*, dystroglycan
268 expression has been reported in different cell types, but surprisingly not in muscle[45]. However,
269 expression of *dgn-1*, one of three worm dystroglycans, has been reported in body wall muscle
270 by single-cell RNA sequencing approaches[28,34]. Consistently, DGN-1 was clearly visible in
271 body wall muscles in our knock-in line, and DGN-1 was colocalized with DYS-1 on the outer
272 face of muscle cells (Figure 3A). Following these observations, we tested whether muscle
273 DGN-1 also required the extracellular matrix protein perlecan[46], dystrophin[47] and
274 dystrobrevin[48] for its surface expression as reported in vertebrates. Indeed, we could observe
275 a profound disruption of DGN-1 surface expression in *dys-1 unc-52*/perlecan and mutants
276 (Figures S2A and S2B). Loss of *dyb-1*/dystrobrevin alone had not effect, and a concomitant
277 loss of *dys-1* and *dyb-1* had no additional effect compared to *dys-1* alone (Figure S2B). While
278 the requirement of dystrobrevin may therefore not be conserved in worms, these results show
279 a clear link between dystroglycan/DGN-1 and dystrophin/DYS-1 in *C. elegans* muscle.
280 To precisely analyse DGN-1 distribution, we used the dense body marker, PAT-2/α-
281 integrin, as a cellular landmark [49]. Double labelling showed that both proteins occupy distinct
282 membrane domains. Indeed, DGN-1 was excluded from dense bodies and M lines occupied
283 by PAT-2 (Figures 3B, 3C and 3D), even using diffraction-limited light microscopy. Dystrophin
284 and dystroglycan are thus present throughout the sarcolemma of worm muscle cells, and
285 occupy specific membrane nanodomains, juxtaposed to integrin-containing attachment sites.
286 Sarcoglycans/Sgc are the other major integral membrane component of the DAPC. The
287 Sgc complex is composed of several sarcoglycan subunits (α, β, γ, δ) in skeletal and cardiac
288 muscles [50]. The *C. elegans* genome encodes three sarcoglycans, *sgca-1*, *sgcb-1*, and *sgn-1*,
289 which are orthologs of α-, β-, and δ/γ-sarcoglycan, respectively[44]. These three genes are co-
290 expressed in worm muscles according to previous reports[38] and transcriptomic data[28]. Using
291 knockin lines, we confirmed their muscular expression and found that sarcoglycans are strictly
292 co-localized (Figures S2C and S2D). As in vertebrates [50], sarcoglycan complex formation and
293 membrane targeting was strongly impaired by the removal of individual subunits (Figure S2E),
294 dystrobrevin or dystrophin (Figure S2F).

295 Interestingly, sarcoglycan distribution was visibly different from DYS-1, as it appeared
296 more confined (Figure 3E), and strongly resembled ISLO-1 (Figures 1D and 1E). Indeed,
297 sarcoglycans are also found at the anterior tip of the muscle cell in a comet-shaped pattern,
298 and cluster into a linear pattern of regularly-spaced punctate microdomains in the posterior
299 part of the cell. These two opposite domains are separated by a small region that appears to
300 be mostly devoid of sarcoglycan (Figure 3F, *gap domain*). By comparing Sgc and PAT-2
301 localization, we could observe that, similarly to dystroglycans, sarcoglycans occupy membrane
302 domains that are clearly juxtaposed to integrin complexes (Figure 3F). Remarkably, we could
303 observe incomplete colocalization between DGN-1 and Sgc whereby some DGN-1 puncta
304 were devoid of sarcoglycan – and vice-versa – (Figure 3G), which suggests the existence of
305 DAPCs with different protein compositions and demonstrates a further level of molecular
306 complexity of the worm's sarcolemma.
307 Furthermore, we analysed the distribution of DYB-1/dystrobrevin, and the two worm
308 syntrophins, STN-1 and STN-2. By comparing their subcellular distributions with DGN-1 and
309 SGCB-1, we could see that they display two distinct localization patterns (Figures S3 and S4).
310 Indeed, STN-2 was broadly expressed and colocalized precisely with DGN-1, while STN-1 and
311 DYB-1 reproduced the more confined distribution pattern of sarcoglycans. Finally, by using
312 TWK-28 as a landmark, we confirmed that all DAPC proteins were colocalized with the channel
313 at the anterior tip of muscle cells (Figure S5).
314 In conclusion, this analysis has revealed that DAPC proteins define multiple membrane
315 subcompartments on the surface of muscle cells, distinct from integrin attachment sites.
316 Moreover, the asymmetrical arrangements of these proteins in individual muscle cells create
317 planar-polarized patterns throughout the muscle tissue.
318
319 **Dishevelled/DSH-1 controls the asymmetric distribution of membrane proteins**
320 Our forward genetic screen revealed the requirement of DAPC proteins for stabilizing TWK-28
321 channels at the cell surface and lead us to uncover the polarized organization of the DAPC
322 itself. Nevertheless, it did not elucidate the specific mechanisms governing muscle cell
323 polarization.
324 Several molecular pathways are known to generate tissue polarity in different cellular
325 contexts. Generally, these involve Wnt ligand/receptor systems and specific proteins belonging
326 to the core planar cell polarity (PCP) pathway[3]. We hypothesized that the polarized
327 organization of TWK-28 could also result from the activity of such tissue polarity pathways,
328 and undertook a candidate gene approach targeting Wnt and PCP genes that are conserved
329 in *C. elegans*[9,25].
330 The intracellular effector dishevelled is a central player in these molecular cascades as
331 it mediates both canonical and non-canonical Wnt signalling[51]. The *C. elegans* genome
332 encodes three dishevelled orthologs: *dsh-1*, *dsh-2,* and *mig-5*. While mutation of *mig-5* or *dsh-*
333 *2* had no defect (Figure S6A), when we combined a *dsh-1* null mutant with the fluorescent
334 SLO-1, TWK-24, and TWK-28 knock-in lines, we observed a striking reorganization of the
335 channels at the muscle surface, leading to a loss of their asymmetric distribution (Figures 4A
336 and 4B). In particular, TWK-28 channels were now found at both extremities of the cell, giving
337 rise to a head-to-tail configuration of anterior and posterior comets in adjacent muscle cells.
338 SLO-1 and TWK-24 distribution was also clearly modified as their domains shifted to a more
339 central position in each cell.
340 To precisely analyze this redistribution, we measured the position – relative to the
341 length of a given muscle cell – of the boundaries between membrane domains that included
342 or that were devoid of channels (Figure 4C).

First, we found that the anterior border was unchanged in *dsh-1(0)* mutants in each case. TWK-28 channels covered on average 30% of the anterior portion of the cell, while SLO-1 and TWK-24 boundaries were more anterior (23% and 21% respectively) and therefore overlapped slightly with the TWK-28 domain.

In contrast, the posterior borders underwent significant displacement. In wild type, sporadic clusters of TWK-28 channels could sometimes be observed at the cell's posterior end, while in *dsh-1(0)* mutants, TWK-28 channels covered over 25% of this region. Thus, anterior and posterior TWK-28 domains were now almost symmetrical. As for SLO-1, the posterior boundary that generally extended almost to the end of the cell, now shifted anteriorly, uncovering close to a fourth of the posterior portion of the cell. Conversely, the TWK-24 domain extended further posteriorly in *dsh-1(0)*, closely aligning with the distribution of SLO-1. Image segmentation of triple-labeled cells demonstrated that even in diffraction-limited conditions, the three channels remained optically separable. This suggests that they still form physically distinct nano-domains within the sarcolemma when muscle polarity is disrupted (Figure 4D).

Next, we wondered whether the redistribution of TWK-28 channels also affected their surface expression levels. Through *in vivo* fluorescence measurements, we determined that the overall quantity remained constant in *dsh-1* mutants. Indeed, TWK-28 fluorescence was now divided between anterior and posterior comets, aligning with the size of each domain (Figure 4E). These data thus suggest that the number of TWK-28 channels present at the cell surface is limited and finely regulated by mechanisms that operate independently of dishevelled/*dsh-1*.

Considering the necessity of dystrophin for TWK-28 surface expression, we postulated that the distribution of DYS-1 would also be modified in *dsh-1* mutants. Using TWK-28 as a landmark, we could clearly observe that dystrophin was indeed present at both extremities of muscle cells (Figure 4F) in a *dsh-1* null mutant. Likewise, the sarcoglycan SGCB-1 displayed a symmetrical distribution pattern, further reinforcing the idea that *dsh-1* plays a major role in ensuring the polarity of muscle cells (Figure 4G).

Lastly, to further investigate the interplay between processes that control TWK-28 surface distribution via dystrophin and DSH-1, we used the TWK-28 mutant lacking the C-terminal PDZ-binding sequence (Figure 2C), as it decouples TWK-28 from the DAPC. In this context, we could detect TWK-28 channels at the anterior and posterior ends in *dsh-1* null mutants (Figure 4H), arguing that TWK-28 channel are addressed to the extremities of muscles cells independently of their interaction with the DAPC, and that the DAPC likely serves to stabilize TWK-28 at the surface in a second step.

Taken together, these data support a model in which DSH-1 ensures that dystrophin and TWK-28 are not addressed or maintained at the posterior end of muscle cells, while the DAPC, subsequently and independently, stabilizes TWK-28 channels at the cell surface. The process that addresses DYS-1, SGCB-1, and TWK-28 to the extremities of muscle cells remains to be determined.

The DIX domain of DSH-1 is dispensable for TWK-28 asymmetry

Dishevelled proteins consist of three conserved functional domains: DIX, PDZ and DEP (Figure 5A). Generally, DIX and PDZ domains are required for canonical Wnt β-catenin signalling, whereas PDZ and DEP domains function in PCP[51]. To investigate which pathways may act downstream of DSH-1 in muscle cells, we expressed a series of protein truncations in body wall muscle cells and monitored the rescue of TWK-28 localization in a *dsh-1* mutant background (Figure 5B).

First, we verified that a *dsh-1a* cDNA was sufficient to restore TWK-28 localization (i.e., panel "+ *Pmyo-3::dsh-1a*"). Next, we expressed truncated *dsh-1a* cDNAs lacking each domain using the same muscle-specific promoter, and found that only the cDNA lacking the DIX domain restored TWK-28 localization in a *dsh-1* null mutant. In line with the absence of a DIX domain requirement, the distribution of TWK-28 remained unaffected in a *bar-1*/β-catenin mutant (Figure S6B).

Taken together, these results show that DSH-1 likely does not engage canonical β-catenin-dependent signalling in this context and point to an involvement of a PCP-type pathway.

Sarcolemmal asymmetry requires Wnt/Ror but not PCP proteins

Based on the findings from our DSH-1 structure-function analysis, we examined the potential participation of genes associated with two planar polarity pathways: the core PCP proteins, VANG-1/Stan, FMI-1/Flamingo, and PRKL-1/Prickle, and the global proteins, CDH-1/Dachsous and CDH-3/CDH-4/Fat. Surprisingly, none of these genes were required for planar-polarized TWK-28 localization (Figure S6B).

Given these results, we investigated the involvement of Wnt-dependent pathways. First, we tested a viable *mig-14*/Wntless hypomorphic mutant that reduces the secretion of Wnt ligands and found that it led to a loss of TWK-28 polarity (Figure 5D). Next, we analyzed viable mutants for four Wnt ligands. We found that only *egl-20* altered the localization of TWK-28 (Figures 5C and S6C). Finally, we tested five transmembrane proteins that bind Wnt ligands: LIN-17, MIG-1, CFZ-2, LIN-18/Ryk and the receptor tyrosine kinase CAM-1/Ror. *lin-17* and *lin-18*, alone, and *mig-1 cfz-2* double mutants had no effect (Figures S6C and S6D). However, *cam-1* mutants phenocopied *egl-20* (Figures 5C and 5E). To confirm these results, we generated an early stop codon at position Pro21 in EGL-20 using CRISPR/*Cas9* gene editing (Figure S6C) and analysed three additional *cam-1* alleles (*ak37*, *cw82*, *ks52*) (Figures 5D and 5E). These four additional mutant alleles all showed phenotypes identical to the reference alleles.

Observing the impact of these gene mutations in more detail along the entire length of the animal provided some additional information about the molecular actors upstream of dishevelled. Specifically, *egl-20* and *cam-1* mutants only affected the distribution of TWK-28 in muscle cells located posteriorly to the vulva. In contrast, *dsh-1 and mig-14* mutation also impacted muscle cells situated more anteriorly (Figure 5C).

This spatially-restricted effect is consistent with the known range of the EGL-20 gradient that is formed by secretion from cells in the tail of the worm, extending to the midbody[19,20]. Furthermore, loss of CAM-1 also did not affect cells anterior to the vulva, which could indicate that a different Wnt receptor/ligand combination is acting in these cells, or that redundant pathways control muscle polarity in the anterior half of the worm.

DSH-1 is asymmetrically localized in body wall muscle cells

To gain further insight into how DSH-1 controls muscle polarity, we analysed the subcellular distribution of DSH-1 using three translational knockin lines in which the mNeonGreen coding sequence was inserted at the N- and C-terminus, and between the DIX and PDZ domains[49].

To validate the functionality of these DSH-1 chimeras tagged with mNeonGreen, we used TWK-28 localization as an indicator of DSH-1 function. Interestingly, while all three lines exhibited comparable fluorescence patterns, only the N- and C-terminal insertions displayed complete functionality. In contrast, the line with an intra-molecular insertion showed mislocalization of TWK-28 channels (data not shown).

438 Using the C-terminally tagged *dsh-1* allele (*bab365*), we analysed the distribution of
439 DSH-1 proteins within muscle cells. Remarkably, DSH-1 was enriched in the posterior third of
440 each body wall muscle cell (Figures 6A and 6B), clearly distinct of TWK-28's anterior
441 localization (Figures 6C). This pattern was lost in *cam-1* and *egl-20* mutants (Figures S7A)
442 suggesting a link between DSH-1 localization and EGL-20/CAM-1 signalling. Surprisingly,
443 while *egl-20* disrupted DSH-1 localization only in muscle cells that were posterior to the vulva—
444 consistent with the EGL-20 gradient—, loss of *cam-1* appeared to affect DSH-1 distribution all
445 along the body. Yet, TWK-28 asymmetry was not affected in *cam-1* mutants anterior to the
446 vulva, while loss of *dsh-1* altered TWK-28 polarization in these cells. Further experiments will
447 be necessary to reconcile these observations.
448
449 **DSH-1 is continuously required to establish and maintain muscle membrane polarity**
450 Next, we wondered whether muscle polarity was a fixed or a dynamic state, i.e., whether DSH-
451 1 was only required to establish muscle polarity initially, or also to maintain it throughout the
452 life to the worm. Therefore, in addition to mNeonGreen, we inserted the AID degron sequence
453 into our DSH-1-mNeonGreen knockin line to be able to manipulate DSH-1 protein levels and
454 study its temporal window of action.
455 First, to validate this approach, we exposed fourth stage (L4) larvae to auxin and
456 – three days later – analysed their F1 progeny at the L4 stage. Using a transgenic line
457 expressing the TIR1 ubiquitin ligase ubiquitously[52], we could observe a robust degradation of
458 DSH-1-AID-mNeonGreen and a clear redistribution of TWK-28 channels into a symmetrical
459 pattern, phenocopying a *dsh-1* null mutant (Figure S7B).
460 Next, to determine the appropriate time window for DSH-1 degradation, we observed
461 the localization pattern of TWK-28 during the first three larval stages, in wild-type and *dsh-1(0)*
462 worms (Figure 6D). While muscle polarity was fully established at the second (L2) and third
463 (L3) larval stages, we observed both polarized and non-polarized cells in freshly-hatched (L1)
464 larvae. Notably, this suggests that TWK-28 polarity is mostly established during
465 embryogenesis, and that it likely derives from an initially non-polarized state.
466 We also observed a progressive change in the shape of TWK-28-containing comets.
467 Only a small number of fluorescent clusters were observed in the L1. However, in the L2 and
468 L3 stages, the number of clusters increased, accompanied by a widening of the comet over
469 time. Loss of *dsh-1* disrupted muscle polarity at all larval stages (Figure 6D).
470 To determine whether *dsh-1* was required to maintain muscle polarity once it was
471 established, we initiated the degradation of DSH-1-mNeonGreen at the L3 larval stage and
472 examined these worms 72 hours later. This protocol led to a clear loss of TWK-28 asymmetry,
473 underscoring the dynamic nature of muscle polarity and the continuous requirement of DSH-1
474 for its maintenance (Figure 6E).
475 Conversely, we asked whether reinitiating DSH-1 expression post-embryonically could
476 restore muscle polarity, beginning from a non-polarized state. In this case, we exposed animals
477 to auxin until the L3 stage, and monitored the recovery of DSH-1 levels and muscle polarity
478 over 72 hours in the absence of auxin (Figure 6F). As for L4 stage animals (Figure S7B), L3
479 animals exposed to auxin throughout their life showed a clear loss of muscle polarity and an
480 absence of DSH-1-associated fluorescence. In turn, over the course of the 72-hour recovery
481 period, we observed a restoration of the polarized distribution pattern of TWK-28.
482 These two complementary experiments directly demonstrate that DSH-1 is required –
483 thorough the life of the animal – to establish and to maintain the polarity of *C. elegans* muscle
484 cells. This demonstrates that muscle polarity is a dynamic state and that it could be regulated
485 by extracellular signals that impact DSH-1 activity.

DISCUSSION

By analysing the subcellular distribution of potassium channels and proteins linked to the dystrophin-associated protein complex (DAPC), we reveal here the planar-polarized organization of *C. elegans* muscle cells. The diverse distribution patterns of these proteins underscore the complex makeup of the worm's sarcolemma. Despite decades of detailed work on the development, structure and function of *C. elegans* muscle cells[26], this remarkable instance of cellular polarization was entirely unsuspected.

We have shown here that muscle polarity is controlled by the Wnt ligand EGL-20, the Wnt receptor CAM-1/Ror and Dishevelled/DSH-1. Signalling cascades involving these proteins have been shown to regulate neurite outgrowth[53], neuroblast migration[13], acetylcholine receptor dynamics at neuromuscular junctions[54], and contribute to asymmetric cell division in epithelial cells[55]. However, the downstream effectors of these cascades remain largely unknown in *C. elegans*.

Among the different non-canonical Wnt pathways in vertebrates, the homologous Wnt5a-ROR-Dvl pathway has garnered significant attention. Perturbation of this signalling cascade in different animal models leads to tissue morphogenesis defects during embryogenesis. In humans, mutations in Wnt5a, ROR2, and Dishevelled proteins cause brachydactyly type B (BDB) and Robinow syndrome. Also known as Robinow dwarfism or fetal face syndrome, it is a rare genetic disorder with significant morphogenetic abnormalities that primarily affect the development of the bones and other parts of the body[4]. Genetic experiments in mice have demonstrated that loss of Wnt5a is phenocopied by concomitant loss of ROR1 and ROR2 receptors [56]. This study also demonstrated that Wnt5a signalling via Ror receptors leads to Dishevelled phosphorylation *in vivo*. Interestingly, CAM-1 is a known interactor of DSH-1 in worms[53], and we have shown here that *cam-1(ks52)* mutants, which lack the intracellular kinase domain, phenocopy *cam-1* null mutants, suggesting that kinase activity may also be required for muscle polarization, possibly through DSH-1 phosphorylation.

Furthermore, proteomic studies have revealed that Wnt5a-Ror signalling modulates the steady-state protein levels of two downstream targets, the kinesin Kif26b and the LNX family member Pdzrn3. Wnt5a-dependent phosphorylation of these proteins triggers their proteasomal degradation. Degradation of Kif26b alters the migratory behaviour of mesenchymal cells in culture[57]. Similarly, Kif26b regulates endothelial cell polarity by reorganizing and stabilizing the microtubule network to achieve directional cell growth in the developing vascular system[58]. In the retinal vasculature, the E3 ubiquitin ligase Pdzrn3 is required for the coordinated and directional extension of endothelial cell[59]. The abundance of Pdzrn3 is also dynamically regulated by the Wnt5a-Ror cascade, and the phosphorylation of three amino acids within the highly conserved LNX3H domain is required for this process[60].

Consistent with the notion that the Wnt-Ror-Dvl cascade may dynamically control intracellular effectors, a remarkable feature of *C. elegans* muscle polarity is that it is a plastic state. Indeed, *C. elegans* muscle polarity remains visible throughout the life of the cell, much like the sensory organs built by PCP processes in fly epithelia and in the inner ear of vertebrates. However, in contrast to these actin-based structures, membrane proteins are generally subjected to constant turnover. This may explain why the continuous activity of DSH-1 is required to maintain membrane organization and muscle polarity. It will, therefore, be essential to identify the molecular targets of DSH-1 in muscle cells and to identify additional factors required to establish and maintain muscle polarity. Forward genetic screens and

534 candidate gene approaches will be necessary in the future to elucidate the cellular
535 mechanisms that establish and maintain muscle polarity in *C. elegans*.
536 Given the essential role of non-canonical Wnt5a-Ror-Dvl signalling in development and
537 human disease, the mechanisms by which this signalling cascade regulates cell biological
538 functions are still insufficiently understood. Therefore, delineating the molecular actors
539 controlling muscle polarity in *C. elegans* may shed light on the conserved mechanisms and
540 molecular effectors that act downstream of Wnt-Ror non-canonical signalling cascades.
541 PCP proteins are generally distributed asymmetrically within polarized cell, which
542 provides a directional cue to break cell symmetry and establish planar cell polarity. As shown
543 here, muscle polarity does not appear to require PCP proteins – at least not when they are
544 disrupted individually. How could symmetry breakage be achieved in this context?
545 Asymmetric localization of DSH-1 is a frequent feature of polarization processes in
546 different species and cellular contexts. For example, Dishevelled is enriched distally in sensory
547 hair cells of the mammalian organ of Corti[61] and in Drosophila wing epithelial cells[62].
548 Asymmetric distributions of Dishevelled have also been described in RME neurons[63] or
549 between neurites of the bipolar PLM neuron[64] in *C. elegans*. We have shown here that DSH-
550 1 displays a clear asymmetric localization in muscle cells. Based on genetic epistasis tests,
551 this posterior enrichment depends on EGL-20/Wnt and CAM-1/Ror. Yet, CAM-1 is uniformly
552 localized on the lateral membrane of muscle cells (data not shown). Therefore, the posterior
553 enrichment of DSH-1 cannot be simply explained by an asymmetric distribution of CAM-1. It
554 could however result from a graded activation of CAM-1 by the EGL-20 gradient. Interestingly,
555 in the developing mouse limb, the Wnt5a receptor ROR2 also does not display an asymmetric
556 distribution in chondrocytes[65]. Thus, it has been proposed that its polarizing function results
557 from a gradient of activity. Indeed, an instructive gradient of Wnt5a activity in the chondrocyte
558 field is translated into a gradient of Vangl2 activity via the formation of the ROR2 and Vangl2
559 protein complex. A model has therefore been proposed in which ROR2 captures the Wnt5a
560 concentration gradient with a dose-dependent response, resulting in Vangl2 phosphorylation
561 according to the Wnt5a gradient.
562 Based on these observations, it is possible that the posterior-to-anterior oriented EGL-
563 20/Wnt gradient could differentially activate CAM-1/Ror at the posterior end of each muscle
564 cell, and subsequently recruit and activate DSH-1 asymmetrically. Such a model implies that
565 EGL-20 may have an instructive role in establishing the polarity of muscle cells. To test this
566 prediction, it would be interesting to express EGL-20 uniformly and assess whether the
567 gradient provides an instructive or a permissive signal. For instance, it has been shown in this
568 way that the ground polarity of vulval precursors cells is established by the instructive activity
569 of EGL-20 via CAM-1 and VANG-1[22].
570 Recent observations have revealed intriguing asymmetric distribution patterns and
571 functions of the DAPC in other cellular contexts. Precise *in vivo* studies of dystrophin in mouse
572 models have been greatly improved by the generation of GFP-tagged mouse knockin lines.
573 These models have confirmed the broad distribution of dystrophin along the membrane of
574 muscle fibers[66,67] but also revealed a striking enrichment at the extremities of muscle fibers
575 where the functions of dystrophin remain to be fully determined [68].
576 Asymmetric localization of dystrophin has also been described in zebrafish muscles[69].
577 Analysis of a gene trap line that fluorescently labels the endogenous dystrophin protein
578 showed that dystrophin is highly enriched at myosepta –the contact site that separate two
579 somites– forming a repetitive chevron-like structure along the length of the body of the fish.
580 During development, more dystrophin is recruited to this interface, exacerbating the
581 asymmetric organization of dystrophin within growing muscle fibers.

582 In activated rodent muscle stem cells (i.e., satellite cells) dystrophin is located apically
583 in close contact with the extracellular matrix. This polarized distribution of dystrophin regulates
584 the asymmetric division of satellite cells via the recruitment of the serine-threonine kinase
585 Par1b[70].
586 Finally, in drosophila, dystrophin is polarized in epithelial migrating cells, where it is
587 found in the posterior half of cells in a complex pattern, illuminating both the cell cortex and
588 filamentous structures partially aligned with F-actin stress fibers[71]. Functional studies have
589 found that the DAPC promotes planar polarization of integrin clusters and participates in the
590 trafficking of ECM components leading to the formation of polarized fibrils[72].
591 Taken together, these observations and our findings suggest that the DAPC may be at
592 the heart of cellular mechanisms that precisely define subcellular cortical domains, allowing
593 specific functions to be compartmentalized within a single cell, and extending its role beyond
594 that of a mere structural component.
595 Although DAPC proteins are often thought to form a single molecular complex, the
596 situation is more complicated at mammalian neuromuscular junctions where they are all
597 present but not colocalized and not involved in the same functions[73]. Our observations also
598 challenge the notion of a singular DAPC composition.
599 At first glance, DAPC components can be categorized into two groups: one comprising
600 DGN-1, DYS-1, and STN-2, and the other encompassing sarcoglycans, DYB-1, and STN-1.
601 One-to-one colocalization revealed that there is significant, but not complete overlap between
602 both groups. For example, the posterior sarcoglycan puncta coincide with areas of denser
603 DGN-1 signal, which is surrounded by weaker DGN-1-associated fluorescence (Figure 3G).
604 This could be explained by different diffusion kinetics with one predominant population of
605 confined sarcoglycans versus two populations of confined *versus* freely diffusing
606 dystroglycans. Moreover, a heterogeneous organization of dystroglycan- and sarcoglycan-
607 containing complexes is visible in the anterior tip of muscle cells where some DGN-1 puncta
608 are devoid of sarcoglycan, and vice-versa.
609 To definitively clarify DAPC localization in worm muscles and determine the exact
610 molecular makeup of dystrophin-containing nanodomains, it will be essential to transition from
611 diffraction-limited microscopy to super-resolution techniques, as the substantial increase in
612 resolution will clarify the composition of membrane nanodomains and spatial distribution of
613 dystrophin and its associated proteins. Indeed, even when proteins appear co-localized using
614 conventional confocal microscopy, they could still occupy distinct nanodomains. Refining their
615 relative location will reveal the heterogeneity within DAPC complexes at the surface of muscle
616 cells. For example, the two worm syntrophins, STN-1 and STN-2, have distinct and partially
617 overlapping distribution patterns in muscle cells. We have also found that they contribute
618 differently to the surface expression of the potassium channel TWK-28. Fly and vertebrates
619 also co-express multiple syntrophins with different subcellular localizations and functions[74].
620 Thus, understanding the interplay between these two worm syntrophins may provide new
621 leads on the mode of action of syntrophins. In the future, one could employ fluorescence
622 recovery or photoconversion techniques to explore the dynamics of various DAPC components
623 *in vivo*. This approach may unveil both molecular and functional diversity within the complex.
624 Finally, it is also interesting to note the clear separation of DAPC and integrin
625 complexes in worm muscles. Using diffraction-limited microscopy, we could easily distinguish
626 these complexes suggesting that they are situated far from each other. These observations
627 refine previous analyses that suggested a close association with dense bodies in the I-band[75].
628 It thus remains to be determined which molecular partners or scaffolds ensure the highly
629 stereotyped subcellular distribution of DAPC proteins.

Whether and how ion channels are distributed to different domains within muscle cells has been rarely investigated specifically, except for the extensive work regarding the targeting of ligand-gated ion channels to neuromuscular junctions[27]. Based on our analysis of single-cell RNAseq data and other published reports, up to 21 potassium channel subunits are likely co-expressed in body wall muscle cells. By comparing the localization of seven of these, we have uncovered a diversity of situations. For instance, TWK-8 and TWK-18 channels are found throughout the sarcolemma, while TWK-12 and TWK-43 channels are only targeted to the basolateral membrane and muscle arms. Conversely, TWK-28 and TWK-42 channels are only found on the outer side of the muscle cell, facing the epidermis, and not on the lateral membrane or muscle arms. Importantly, the comparison of TWK-28, TWK-24, and SLO-1 channels shows that even when channels are located in the same region of the sarcolemma (i.e., the outer face of the cell), they can occupy distinct –yet partially overlapping– regions along the antero-posterior axis. And even when they are present in overlapping regions, ion channels remain confined to distinct nanodomains. The remarkable consistency of these patterns across various individuals and within the muscle cells of a single animal suggests the existence of precise molecular and cellular mechanisms responsible for directing individual channels to their designated domains, likely endowing them with distinct electrophysiological properties.

Another remarkable observation is the difference in organization of TWK-28, ISLO-1 and SLO-1 (Figure 1). ISLO-1's interaction with SLO-1 and the syntrophin STN-1 recruits the BK potassium channel to the DAPC. In turn, mutations in *islo-1* and *dys-1* have been demonstrated to disrupt the surface expression of SLO-1 within muscle cells[36]. Yet, we have shown here that ISLO-1 and SLO-1 localization patterns are not identical since ISLO-1 is also present in the comet-shaped domain at the anterior tip of each muscle cell. Similarly, we have found that *islo-1, dys-1* and syntrophins are necessary for TWK-28 surface expression. Yet, TWK-28 is restricted to the anterior domain. Notably, even when cellular polarity is disrupted by mutations in *egl-20*/Wnt, *cam-1*/Ror and *dsh-1/*Dishevelled, the posteriorly-localized TWK-28 does not reproduce the posterior, punctate, ISLO-1 pattern, but rather mirrors the comet-shaped distribution seen at the anterior tip in wild-type animals. Therefore, there are likely other factors that allow the selective recruitment of TWK-28 and SLO-1 to distinct anterior and posterior domains. An important question in the future will be to understand the functional implications of these specific ion channel distributions on the control of muscle excitability and contraction.

ACKNOWLEDGEMENTS

We thank Hannes Bülow, Jean-Louis Bessereau, Vincent Mirouse, Bénédicte Durand and Martin Harterink for critical reading and comments about the manuscript. We are grateful to Terese Lawry and Martin Chalfie for sharing *C. elegans* strains. We thank Driss Laabid for technical assistance. This work was funded by grants to T.B. from the European Research Council (ERC Stg 2013, *Kelegans*), AFM Téléthon (Alliance MyoNeurALP), and ANR (AAPG 2023, *DYSCO*). A.P. was supported by AFM Téléthon and LabEx CORTEX. We thank *Le Centre d'Imagerie Quantitative Lyon-Est* (LyMIC-CIQLE, Lyon, France) imaging facility for support and access to equipment. Some strains were generated by SEGiCel (SFR Santé Lyon Est CNRS UAR 3453, Lyon, France). Some strains were provided by the CGC, which is funded by NIH Office of Research Infrastructure Programs (P40 OD010440). Some strains were provided by the National Bioresource Project at the Tokyo Women's Medical University School of Medicine, which is part of the International *C. elegans* Gene Knockout Consortium.

AUTHOR CONTRIBUTIONS

A. P., N. Z., M. G., A. C.-L., N. F., and E. C. performed experiments in *C. elegans*. O.A. performed two-electrode voltage-clamp experiments. All authors were involved in the analysis of the experimental data. T. B. supervised the work. A. P. and T. B. wrote the manuscript.

COMPETING INTERESTS

The authors declare no competing financial interests.

MATERIALS & METHODS

DATA AVAILABILITY

Worm strains and plasmids generated in this study are available upon request. Source data are provided with this paper. Further information and requests for resources and reagents should be directed to and will be fulfilled by Thomas Boulin.

EXPERIMENTAL MODEL AND SUBJECT DETAILS

Strains and genetics

All *C. elegans* strains were originally derived from the wild-type Bristol N2 strain. Worm cultivation, genetic crosses, chemical mutagenesis and manipulation of *C. elegans* were carried out according to standard protocols[76]. All strains were maintained at 20°C on nematode growth medium (NGM) agar plates with *Escherichia coli* OP50 as a food source. Strains and alleles used for this study are listed in Supplementary Table S1 and S2, respectively.

METHOD DETAILS

Molecular biology

Single-strand oligonucleotides, crRNA, and plasmids used in this study are described in Supplementary Table 3, 4, and 5, respectively.

Auxin-induced degradation

Auxin plates were prepared by adding auxin Indole-3-Acetic Acid (Sigma) from a 400 mM stock solution in ethanol into NGM at the final concentration of 1 mM[43]. DYS-1 and DSH-1 degradation was performed using a transgene expressing TIR1 with the ubiquitous promoter *Peft-3*[52]. Protein degradation was monitored *in vivo* based on mNeonGreen fluorescence.

Microscopy imaging and quantification

General methods Freely moving worms were observed on nematode growth media (NGM) plates using an AZ100 macroscope (Nikon) equipped with a Flash 4.0 CMOS camera (Hamamatsu Photonics). For confocal imaging, animals were mounted on 2% dry agarose pads with 2% polystyrene beads (Tebu-Bio, polystyrene polybeads 0.10 µm microsphere) in M9 buffer (3 g KH_2PO_4, 6 g Na_2HPO_4, 5 g NaCl, 0.25 g $MgSO_4 \cdot 7\ H_2O$, and distilled water up to 1 litre). Confocal imaging was performed using an inverted confocal microscope (Olympus IX83) equipped with a confocal scanner unit spinning-disk scan head (Yokogawa) and an EMCDD camera (iXon Ultra 888, Andor) at the Ciqle imaging facility (Centre d'Imagerie Quantitative Lyon-Est, LyMIC-CIQLE, Lyon, France).

TWK-28-mNeonGreen fluorescence intensity quantification Quantification of fluorescent images was performed using ImageJ (version: 2.0.-rc-69/1.53a). Each data point represents

726 one muscle cell and data from at least three independent imaging sessions were pooled for
727 each genotype. Acquisition parameters were the same across genotypes for quantitative
728 analyses. Fluorescence intensity was measured for Figure 2A to 2E in a region of interest of
729 30 µm (long) x 5 µm (wide) x 2.5 µm (deep), and for Figure 2J in a region of interest of 50 µm
730 (long) x 5 µm (wide) x 2.5 µm (deep). To quantify the fluorescence intensity of TWK-28 in figure
731 4E, we first segmented individual muscle cells using TWK-12::wrmScarlet to outline the muscle
732 membrane. The total fluorescence intensity was corrected by subtracting background
733 fluorescence from the middle of the cell, where TWK-28 was undetectable.
734
735 ***Measurement of TWK-28, TWK-24 and SLO-1 domain boundaries*** To determine the
736 precise outline of individual muscle cells, we used TWK-12::wrmScarlet for cell membrane
737 segmentation. We then measured the length of each cell and the relative position of the TWK-
738 28, TWK-24 and SLO-1 domain boundaries along the antero-posterior axis using ImageJ
739 (Figure 4C).
740
741 **Electrophysiology and heterologous expression of TWK-28 in *Xenopus laevis* oocytes**
742 Capped mRNAs were synthesized in vitro from linearized expression vectors using the T7
743 mMessage mMachine kit (Ambion, Austin, TX, USA). Defolliculated *X. laevis* oocytes (Ecocyte
744 Bioscience, Dortmund, Germany) were injected with 50 nL containing 1.8 ng of cRNA. Oocytes
745 were kept at 18°C in ORII Calcium solution containing (in millimolar): 82.5 NaCl, 2 KCl, 1
746 $MgCl_2$, 0.7 $CaCl_2$, 5 HEPES, gentamicin (25 µg/mL), pH 7.5 (with TRIZMA-Base).
747 Two-electrode voltage clamp (TEVC) experiments were performed 24 hours after
748 microinjection. Oocytes were mounted in a small home-made recording chamber and
749 continuously superfused with ND96 solution containing (in millimolar): 96 NaCl, 2 KCl, 1.8
750 $CaCl_2$, 2 $MgCl_2$, 5 HEPES. pH 7.4 was adjusted with Trizma base. Macroscopic currents were
751 recorded using a Warner Instrument OC-725 amplifier, filtered at 10kHz, digitized using a
752 Digidata-1322 (Axon Instrument). For current visualization and stimulation protocol application,
753 we used Axon pClamp 9 software (Molecular Devices, Sunnyvale, CA). Recording electrodes
754 were pulled to 0.2-1.0 MΩ by using a horizontal puller (Sutter Instrument, Model P-97, USA)
755 and filled with 3 M KCl. Currents were recorded in response to a voltage-step protocol
756 consisting of a pre-pulse of -80 mV (80 ms duration) from a holding potential of -60 mV,
757 followed by 10 mV steps (200 ms duration) from -150 mV to +50 mV, and return to a -60 mV
758 holding potential. Current-voltage curves were obtained by plotting the steady-state currents
759 at the end of each voltage step.
760
761 **QUANTIFICATION AND STATISTICAL ANALYSIS**
762 In *dsh-1, mig-14, egl-20 and cam-1* mutant animals, polarity was assessed in more than 25
763 animals for each genotype, and scored as defective when more than four cells were found to
764 be symmetrical. Conversely, we considered that a given *dsh-1* cDNA was functionally sufficient
765 to rescue muscle polarity if the *dsh-1* polarity defect was reversed in more than four cells of
766 more than ten transgenic animals.
767 The statistical analysis was performed using the R software package. Normality of sample
768 distributions was assessed using the Shapiro-Wilks normality test before choosing parametric
769 (Student's *t* test) or a non-parametric (Mann-Whitney) tests, as indicated in relevant figure
770 legends. Graphs were plotted using the PlotsOfData service[77].
771

FIGURE LEGENDS

Figure 1. Ion channel localization reveals polarized muscle membrane compartmentalization

(A) Schematic diagram of the organization of the *C. elegans* musculature in the head, the midbody region, and in a cross section. Head and midbody dorso-ventral views show two out of four muscle quadrants. Successive muscle cells are labelled in green and dark grey. Anterior (*Ant*) to the left, posterior (*Pos*) to the right. Dorsal and ventral nerve cords are labelled in blue in the cross-section. Epidermal tissue is coloured in light grey.

(B) Asymmetric localization of TWK-28, TWK-24 and SLO-1 channels. Muscle membrane labelled by TWK-12-wrmScarlet, magenta.

(C) Image segmentation reveals little to no co-localization of ion channels in triple-labelled muscle cells using TWK-28 (cyan), TWK-24 (magenta), and SLO-1(green) fluorescent knockin lines.

(D) SLO-1 and ISLO-1 distributions coincide exclusively in the posterior domain. ISLO-1 is also found in the anterior domain of the muscle cell.

(E) TWK-28 and ISLO-1 distributions overlap in the anterior domain of muscle cells. Rightmost column, magnified view of anterior domain of a muscle cell.

Regions of interest in (D) and (E): *Anterior domain*, comet-shaped domain at anterior tip of muscle cells; *Posterior domain,* punctate clustered pattern in posterior part of muscle cells.

Muscle cell outlines are indicated with yellow dashed lines. Scale bars, 20 µm.

Figure 2. Dystrophin and DAPC proteins determine TWK-28 content in the anterior domain of muscle cells

(A) Confocal detection and quantification of mNeonGreen-TWK-28 in a long-isoform-specific *dys-1* mutant *(bln582)* and a *dys-1* molecular null allele *(syb2174)*.

(B) Confocal detection and quantification of mNeonGreen-TWK-28 in *dyb-1(cx36)* and *islo-1(bln549)* loss-of-function mutants.

(C) C-terminal sequence of the TWK-28ΔPDZ variant engineered by gene editing of mNeonGreen-TWK-28 to eliminate a putative PDZ-binding motif (orange residues).

(D) Confocal detection and quantification of mNeonGreen-TWK-28 in *stn-1(ok292)* and *stn-2(ok2417)* loss-of-function mutants, and of an mNeonGreen-TWK-28 knockin line lacking the final four C-terminal amino acids (*twk-28ΔPDZ*).

(E) Confocal detection and quantification of mNeonGreen-TWK-28 and mNeonGreen-*twk-28ΔPDZ* in a *dys-1(syb2174)* mutant background.

(F) DYS-1 degradation protocol. L4 (P0) worms are transferred to auxin-containing media at day 0 (D0). F1 progeny are exposed to auxin until the L4 stage (ON Auxin) and transferred to NGM plates (OFF Auxin) for 24 h. Confocal detection and quantification of fluorescence at day 3 (D3) and 24 hours later (D3 + 24 h).

(G) DYS-1-AID-mNeonGreen is strongly degraded after lifelong exposure to auxin (ON Auxin, D3). Partial recovery 24 h after removal from auxin (OFF Auxin, D3 + 24h).

(H), (I) Confocal detection of wrmScarlet-TWK-28 and DYS-1-AID-mNeonGreen at D3 and D3 + 24h, in the absence of auxin (NO Auxin, age-matched controls), after auxin exposure for three days (ON Auxin), and after removal from auxin for 24 h (OFF Auxin).

(J) Quantification of wrmScarlet-TWK-28 fluorescence shown in (H) and (I).

Statistical tests: Kruskal-Wallis with Dunn's multiple comparison post hoc test; Mann-Whitney test (for J). n > 30 in all samples; n.s., not significant, * $p < 0.05$

Scale bars, 20 µm

820
821 **Figure 3. Dystrophin, dystroglycan and sarcoglycans define asymmetrical membrane**
822 **compartments at the surface of *C. elegans* muscle cells**
823 (A) DGN-1 and DYS-1 distributions overlap in body wall muscle cells.
824 (B) DGN-1 localizes to membrane domains devoid of α-integrins/PAT-2. Representative
825 images of head muscle cells of translational fusion knockin lines for DGN-1-wrmScarlet (in
826 magenta) and PAT-2-mNeonGreen (in green).
827 (C), (D) DGN-1 and PAT-2 occupy juxtaposed and optically-separable membrane domains.
828 Enlargement of images shown in panel B.
829 (E) SGCB-1 and DYS-1 distributions overlap only partially in body wall muscle cells.
830 (F) SGCB-1 partitions into distinct membrane domains along the antero-posterior axis of
831 individual muscle cells. *Anterior domain*, comet-shaped domain. *Gap domain,* sparse
832 localization. *Posterior domain,* clustered pattern aligned with, but optically-separable from,
833 PAT-2-labeled dense bodies.
834 (G) DGN-1 and SGCB-1 patterns only partially coincide in the anterior and posterior regions
835 of muscle cells.
836 Muscle cell outlines are indicated with yellow dashed lines. Scale bars, 20 µm.
837
838 **Figure 4. Loss of DSH-1/Dishevelled disrupts the planar-polarized organization of the**
839 **muscle plasma membrane**
840 (A), (B) Symmetrical distribution of TWK-28, SLO-1 and TWK-24 in a *dsh-1(ok1445)* loss-of-
841 function background. Muscle membrane labelled by TWK-12-wrmScarlet (in magenta).
842 (B) Magnified view of single muscle cells in wild type and *dsh-1(ok1445)*.
843 (C) Quantification of TWK-28, SLO-1 and TWK-24 domain boundary positions in wild type and
844 *dsh-1(ok1445)*. Average position of anterior (*Ant*) boundaries in wild type (black) and *dsh-*
845 *1(ok1445)* (red), respectively, as percentages of muscle cell length: TWK-28, 31% and 30%;
846 SLO-1, 24% and 23%; TWK-24, 23% and 21%. Average position of posterior (*Pos)* boundaries
847 in wild type and *dsh-1(ok1445)*, respectively, as percentages of muscle cell length: TWK-28,
848 97% and 73%; SLO-1, 90% and 78%; TWK-24, 68% and 80%. Gray and red bars indicate the
849 region containing each ion channel. Number of cells assayed in each condition: TWK-28 (WT,
850 n=29; *dsh-1*, n=25); SLO-1 (WT, n=30; *dsh-1*, n=26); TWK-24 (WT, n=33; *dsh-1*, n=26). Mann-
851 Whitney test, n.s. not significant, * $p < 0.0001$.
852 (D) Image segmentation reveals little to no co-localization of ion channels in *dsh-1*-mutant
853 muscle cell using TWK-28 (cyan), TWK-24 (magenta), and SLO-1(green) fluorescent knockin
854 lines.
855 (E) Total TWK-28 amount is unchanged in *dsh-1(ok1445)* as TWK-28 is redistributed between
856 the anterior and posterior domains. Mann-Whitney test, n.s. not significant, * $p < 0.05$.
857 (F) Symmetrical distribution of DYS-1 and TWK-28 at extremities of muscle cells in *dsh-*
858 *1(ok1445)*.
859 (G) Symmetrical distribution of SGCB-1 in *dsh-1(ok1445)*.
860 (H) Symmetrical distribution TWK-28 lacking the PDZ binding-motif in *dsh-1(ok1445)*. White
861 arrowheads indicate remaining fluorescent signal.
862 Muscle cell outlines are indicated with yellow dashed lines. Scale bars, 20 µm.
863
864 **Figure 5. Loss of MIG-14/Wntless, EGL-20/Wnt and CAM-1/Ror disrupts asymmetric**
865 **localization of TWK-28**
866 (A) Schematic protein structure of DSH-1a including DIX, PDZ, and DEP domains.

867 (B) Muscle-specific expression of full-length or DIX domain-truncated DSH-1a proteins
868 rescues TWK-28 localization in *dsh-1(ok1445)*. PDZ and DEP domains are necessary for
869 DSH-1 function in muscle polarity.
870 (C) Loss of MIG-14/Wntless, EGL-20/Wnt, and CAM-1/Ror disrupts polarized localization of
871 TWK-28. Posterior mid-body muscle cells are affected in all mutant genotypes. In *cam-1* and
872 *egl-20* mutants, polarity is not affected in muscle cells situated anteriorly to the vulva ("Anterior
873 midbody").
874 (D) Schematic protein structure of CAM-1/Ror receptor, with corresponding molecular lesions
875 in point mutants (*gm122* and *cw82)*, and deletion alleles (*ak37* and *ks52*).
876 (E) *cam-1(ak37), cam-1(ks52),* and *cam-1(cw82)* disrupt TWK-28 polarity in posterior mid-
877 body muscles.
878 Left- or right-pointing yellow arrowheads indicate anterior or posterior extremity of muscle cells,
879 respectively. Non-specific intestinal lysosome-related autofluorescence is visible in some
880 panels and labelled with a white asterisk. Scale bars, 20 μm.
881
882 **Figure 6. DSH-1/Dishevelled is required to establish and maintain muscle polarity**
883 (A) Representative micrograph of an mNeonGreen translational knockin line of DSH-1. DSH-
884 1 is enriched in the posterior portion of body wall muscle cells. DSH-1-mNeonGreen is visible
885 in ventral nerve cord motoneuron cell bodies and neurites. Ventral view.
886 (B) DSH-1-mNeonGreen distribution in a single muscle cell. Muscle membrane labelled by
887 TWK-12-wrmScarlet (in magenta). Average position of DSH-1 domain boundary, 72 % of
888 muscle cell length, n=29. *Ant*, anterior; *Pos*, posterior. Gray bar indicates the region containing
889 DSH-1.
890 (C) DSH-1 and TWK-28 are found at opposite ends of muscle cells. Yellow or white
891 arrowheads indicate the anterior or posterior end of muscle cells, respectively. Dashed lines
892 indicate the outline of muscle cells with the same colour code.
893 (D) Asymmetric localization of TWK-28 in L1, L2, and L3 larval stages. Non-polarized muscle
894 cells are found in wild-type at the L1 stage. Loss of *dsh-1* disrupts muscle polarity at all stages.
895 Muscle cells are labelled with cytoplasmic mCherry in the L1 stage and outlined with white
896 dotted lines.
897 (E) DSH-1 is required to maintain muscle polarity during post-embryonic development.
898 (F) Muscle polarity is restored by re-expression of DSH-1 during post-embryonic development.
899 White arrowheads indicate the posterior end of muscle cells in (A), (B), and (C).
900 Left- or right-pointing yellow arrowheads indicate anterior or posterior extremity of muscle cells,
901 respectively. Scale bars, 20 μm.
902

903 **SUPPLEMENTARY FIGURE LEGENDS**
904
905 **Figure S1. Genetic suppression of a TWK-28 L210T gain-of-function mutant by**
906 **mutations in *dys-1* and *islo-1***
907 (A) Two-pore domain potassium channels TWK-8, TWK-18, TWK-24, and TWK-42 expression
908 and subcellular distributions are unchanged in *dys-1(bln582)* loss-of-function mutants.
909 Representative images of head musculature.
910 (B) Two-pore domain potassium channels TWK-12 and TWK-43 are enriched in muscle arms
911 and on the lateral membrane of muscle cells.
912 (C) Current–voltage relationships obtained at pH 7.4 in *X. laevis* oocytes after injection of
913 cRNA encoding TWK-28 wild-type (black squares) and TWK-28 L210T gain-of-function
914 channels (red squares). Inset shows leftward shift of reversal potential in TWK-28 L210T. n=8
915 and n=7 for wild type and TWK-28 L210T, respectively.
916 (D) Low and high magnification micrographs illustrating reduced locomotion and relaxed body
917 posture of TWK-28 L210T gain-of-function mutants on NGM plates.
918 (E) Loss-of-function mutations in *dys-1* and a missense mutation in *islo-1* suppress paralysis
919 of the TWK-28 L210T gain-of-function mutation.
920 (F) TWK-28 localization and levels are unchanged in sarcoglycan single or triple null mutants.
921 (G) Quantification of TWK-28-associated fluorescence. Mann-Whitney test; n.s., not
922 significant.
923 Scale bars, 20 μm
924
925 **Figure S2. Dystrophin is required for sarcolemmal localization of dystroglycan and**
926 **sarcoglycans.**
927 (A) Reduction in surface expression and mislocalization of DGN-1/Dystroglycan in *unc-*
928 *52/*perlecan loss-of-function mutants.
929 (B) DGN-1/Dystroglycan localization is dependent on DYS-1, but not DYB-1.
930 (C), (D) Sarcoglycans SGCA-1 and SGN-1 are colocalized with SGCB-1.
931 (E) Subunit interdependence for surface expression of SGCA-1, SGCB-1 and SGN-1.
932 (F) SGBC-1 localization is disrupted differently in *dys-1* and *dyb-1* mutants.
933 Scale bars, 20 μm.
934
935 **Figure S3. Relative localization of DAPC component in *C. elegans* head muscles**
936 (A) Colocalization of DGN-1 and STN-2.
937 (B) Colocalization of SGCB-1 and DYB-1.
938 (C) Colocalization of SGCB-1 and STN-1.
939 (D) Colocalization of DGN-1 and DYB-1.
940 (E) Colocalization of STN-1 and STN-2.
941 Muscle cell outlines are indicated with yellow dashed lines. Scale bars, 20 μm.
942
943 **Figure S4. DAPC components partition to dystroglycan- or sarcoglycan-containing**
944 **membrane compartments**
945 (A) Colocalization of DGN-1 and DYS-1.
946 (B) Colocalization of DGN-1 and STN-2.
947 (C) Colocalization of SGCB-1 and DYB-1.
948 (D) Colocalization of SGCB-1 and STN-1.
949 (E) Colocalization of DGN-1 and DYB-1.
950 (F) Colocalization of SGCB-1 and DYS-1.

(G) Colocalization of STN-1 and STN-2.
Anterior domain, comet-shaped domain at anterior tip of muscle cells; *Posterior domain,* punctate clustered pattern in posterior part of muscle cells.

Figure S5. TWK-28 colocalizes with all DAPC components

Colocalization of TWK-28 with SGCB-1, STN-1, DYB-1, DGN-1, DYS-1 and STN-2. Rightmost column, magnified view of anterior region of individual muscle cells.
Scale bars, 20 µm.

Figure S6. EGL-20/Wnt is required for muscle cell polarity while several Wnt ligands and receptors are not

(A) Polarized localisation of TWK-28 is unaffected in *mig-5* or *dsh-2* null mutants. Homozygous *dsh-2* mutants were derived from heterozygous parents.
(B) Polarized localisation of TWK-28 is maintained in the absence of core planar cell polarity components (*vang-1, fmi-1, prkl-1*), Cadherin/Fat/Dachsous pathway components (*cdh-1, cdh-3, cdh-4*), or β-catenin (*bar-1*).
(C), (D) Wnt ligands (*cwn-1, cwn-2, lin-44*), frizzled receptors (*lin-17, mig-1, cfz-2*) and the tyrosine kinase-related receptors LIN-18/Ryk are not required for TWK-28 polarization. *egl-20(bln916)* –an early nonsense mutation at position Pro21– disrupts TWK-28 polarity in posterior midbody muscles.
Scale bars, 20 µm.

Figure S7. The localization of DSH-1 is dependent on CAM-1 and EGL-20

(A) Enrichment of DSH-1 at the posterior end of muscle cells is lost in *cam-1* and *egl-20* mutants. DSH-1 localization is however conserved in the anterior midbody of *egl-20* mutants, consistent with the posteriorly-restricted distribution of EGL-20. White arrowheads indicate DSH-1 enrichment at the posterior end of muscle cells. Ventral views.
(B) Life-long degradation (Auxin-treated) of DSH-1-AID-mNeonGreen using a ubiquitous TIR1-expressing transgene disrupts asymmetric localization of TWK-28 in muscle cells. Yellow arrowheads indicate the position and orientation of TWK-28 domains.
Scale bars, 20 µm.

983 **REFERENCES**
984

985 1. Nusse, R. & Clevers, H. Wnt/β-Catenin Signaling, Disease, and Emerging Therapeutic
986 Modalities. *Cell* **169**, 985–999 (2017).

987 2. Butler, M. T. & Wallingford, J. B. Planar cell polarity in development and disease. *Nat Rev*
988 *Mol Cell Bio* **18**, 375–388 (2017).

989 3. Yang, Y. & Mlodzik, M. Wnt-Frizzled/Planar Cell Polarity Signaling: Cellular Orientation by
990 Facing the Wind (Wnt). *Annu Rev Cell Dev Bi* **31**, 623–646 (2015).

991 4. Konopelski Snavely, S. E. *et al.* Non-canonical WNT5A-ROR signaling: New perspectives
992 on an ancient developmental pathway. *Curr. Top. Dev. Biol.* **153**, 195–227 (2023).

993 5. Montcouquiol, M., Crenshaw, E. B. 3rd & Kelley, M. W. Noncanonical Wnt signaling and
994 neural polarity. *Annu Rev Neurosci.* **29**, 363–386 (2006).

995 6. Montcouquiol, M. *et al.* Identification of Vangl2 and Scrb1 as planar polarity genes in
996 mammals. *Nature* **423**, 173–177 (2003).

997 7. Korswagen, H. C. Canonical and non-canonical Wnt signaling pathways in Caenorhabditis
998 elegans: variations on a common signaling theme. *BioEssays* **24**, 801–810 (2002).

999 8. Chen, C.-K. & Pan, C.-L. Cell polarity control by Wnt morphogens. *Dev. Biol.* **487**, 34–41
1000 (2022).

1001 9. Cravo, J. & Heuvel, S. van den. Tissue polarity and PCP protein function: C. elegans as
1002 an emerging model. *Curr Opin Cell Biol* **62**, 159–167 (2020).

1003 10. Sawa, H. & Korswagen, H. C. Wnt signaling in C. elegans. *WormBook* 1–30 (2013)
1004 doi:10.1895/wormbook.1.7.2.

1005 11. Eisenmann, D. M. Wnt signaling. *WormBook* 1–17 (2005) doi:10.1895/wormbook.1.7.1.

1006 12. Shah, P. K. *et al.* PCP and SAX-3/Robo Pathways Cooperate to Regulate Convergent
1007 Extension-Based Nerve Cord Assembly in C. elegans. *Dev. Cell* **41**, 195-203.e3 (2017).

1008 13. Mentink, R. A. *et al.* Cell Intrinsic Modulation of Wnt Signaling Controls Neuroblast
1009 Migration in C. elegans. *Dev. Cell* **31**, 188–201 (2014).

1010 14. Rella, L., Póvoa, E. E. F. & Korswagen, H. C. The Caenorhabditis elegans Q
1011 neuroblasts: A powerful system to study cell migration at single-cell resolution in vivo.
1012 *genesis* **54**, 198–211 (2016).

1013 15. Steimel, A. *et al.* The Flamingo ortholog FMI-1 controls pioneer-dependent navigation of
1014 follower axons in C. elegans. *Development* **137**, 3663–3673 (2010).

1015 16. Chien, J., Devkota, R., Yosef, N. & Mörck, C. Regulation of Axon Guidance by the Wnt
1016 Receptor Ror/CAM-1 in the PVT Guidepost Cell in Caenorhabditis elegans. *Genetics* **207**,
1017 1533–1545 (2017).

1018 17. Zheng, C., Diaz-Cuadros, M. & Chalfie, M. Dishevelled attenuates the repelling activity of
1019 Wnt signaling during neurite outgrowth in Caenorhabditis elegans. *Proc. Natl. Acad. Sci.* **112**,
1020 13243–13248 (2015).

1021 18. Chen, C.-H., He, C.-W., Liao, C.-P. & Pan, C.-L. A Wnt-planar polarity pathway instructs
1022 neurite branching by restricting F-actin assembly through endosomal signaling. *PLoS Genet.*
1023 **13**, e1006720 (2017).

1024 19. Coudreuse, D. Y. M., Roël, G., Betist, M. C., Destrée, O. & Korswagen, H. C. Wnt
1025 Gradient Formation Requires Retromer Function in Wnt-Producing Cells. *Science* **312**, 921–
1026 924 (2006).

1027 20. Pani, A. M. & Goldstein, B. Direct visualization of a native Wnt in vivo reveals that a long-
1028 range Wnt gradient forms by extracellular dispersal. *Elife* **7**, e38325 (2018).

1029 21. Goldstein, B., Takeshita, H., Mizumoto, K. & Sawa, H. Wnt Signals Can Function as
1030 Positional Cues in Establishing Cell Polarity. *Dev. Cell* **10**, 391–396 (2006).

1031 22. Green, J. L., Inoue, T. & Sternberg, P. W. Opposing Wnt Pathways Orient Cell Polarity
1032 during Organogenesis. *Cell* **134**, 646–656 (2008).

1033 23. Hoffmann, M., Segbert, C., Helbig, G. & Bossinger, O. Intestinal tube formation in
1034 Caenorhabditis elegans requires vang-1 and egl-15 signaling. *Dev. Biol.* **339**, 268–279
1035 (2010).

1036 24. Lavalou, J. & Lecuit, T. In search of conserved principles of planar cell polarization. *Curr.*
1037 *Opin. Genet. Dev.* **72**, 69–81 (2022).

1038 25. Ackley, B. D. Wnt-signaling and planar cell polarity genes regulate axon guidance along
1039 the anteroposterior axis in C. elegans. *Dev. Neurobiol.* **74**, 781–796 (2014).

1040 26. Gieseler, K., Qadota, H. & Benian, G. M. *Development, Structure, and Maintenance of C.*
1041 *Elegans Body Wall Muscle*. 1–59 (2017).

1042 27. Mizumoto, K., Jin, Y. & Bessereau, J.-L. Synaptogenesis: unmasking molecular
1043 mechanisms using Caenorhabditis elegans. *Genetics* **223**, (2023).

1044 28. Cao, J. *et al.* Comprehensive single-cell transcriptional profiling of a multicellular
1045 organism. *Science* **357**, 661–667 (2017).

1046 29. Vigne, P. *et al.* A single nucleotide change underlies the genetic assimilation of a plastic
1047 trait. *bioRxiv* 2020.06.29.176990 (2020).

1048 30. Kunkel, M. T., Johnstone, D. B., Thomas, J. H. & Salkoff, L. Mutants of a temperature-
1049 sensitive two-P domain potassium channel. *The Journal of neuroscience : the official journal*
1050 *of the Society for Neuroscience* **20**, 7517–7524 (2000).

1051 31. Cruz, I. P. de la, Levin, J. Z., Cummins, C., Anderson, P. & Horvitz, H. R. sup-9, sup-10,
1052 and unc-93 may encode components of a two-pore K+ channel that coordinates muscle
1053 contraction in Caenorhabditis elegans. *Journal of Neuroscience* **23**, 9133–9145 (2003).

1054 32. El Mouridi, S. *et al.* Reliable CRISPR/Cas9 Genome Engineering in Caenorhabditis
1055 elegans Using a Single Efficient sgRNA and an Easily Recognizable Phenotype. *G3 Genes*
1056 *Genomes Genetics* **7**, 1429–1437 (2017).

1057 33. Oh, K. H. *et al.* ERG-28 controls BK channel trafficking in the ER to regulate synaptic
1058 function and alcohol response in C. elegans. *eLife* **6**, e1001077 (2017).

1059 34. Taylor, S. R. *et al.* Molecular topography of an entire nervous system. *Cell* **184**, 4329-
1060 4347.e23 (2021).

1061 35. Carre-Pierrat, M. *et al.* The SLO-1 BK channel of Caenorhabditis elegans is critical for
1062 muscle function and is involved in dystrophin-dependent muscle dystrophy. *J Mol Biol* **358**,
1063 387–395 (2006).

1064 36. Kim, H. *et al.* The Dystrophin Complex Controls BK Channel Localization and Muscle
1065 Activity in Caenorhabditis elegans. *Plos Genet* **5**, e1000780 (2009).

1066 37. Sancar, F. *et al.* The dystrophin-associated protein complex maintains muscle excitability
1067 by regulating Ca(2+)-dependent K(+) (BK) channel localization. *Journal of Biological*
1068 *Chemistry* **286**, 33501–33510 (2011).

1069 38. Kim, H. *et al.* The dystrophin complex controls bk channel localization and muscle activity
1070 in Caenorhabditis elegans. *PLoS Genetics* **5**, e1000780 (2009).

1071 39. Ben Soussia, I. *et al.* Mutation of a single residue promotes gating of vertebrate and
1072 invertebrate two-pore domain potassium channels. *Nature communications* **10**, 787 (2019).

1073 40. Connors, N. C., Adams, M. E., Froehner, S. C. & Kofuji, P. The Potassium Channel
1074 Kir4.1 Associates with the Dystrophin-Glycoprotein Complex via α-Syntrophin in Glia*. *J Biol*
1075 *Chem* **279**, 28387–28392 (2004).

1076 41. Gavillet, B. *et al.* Cardiac Sodium Channel Nav1.5 Is Regulated by a Multiprotein
1077 Complex Composed of Syntrophins and Dystrophin. *Circ Res* **99**, 407–414 (2006).

1078 42. Hui, S., Xing, X. & Bader, G. D. Predicting PDZ domain mediated protein interactions
1079 from structure. *Bmc Bioinformatics* **14**, 27 (2013).

1080 43. Zhang, L., Ward, J. D., Cheng, Z. & Dernburg, A. F. The auxin-inducible degradation
1081 (AID) system enables versatile conditional protein depletion in C. elegans. *Development* **142**,
1082 4374–4384 (2015).

1083 44. Grisoni, K., Martin, E., Gieseler, K., Mariol, M.-C. & Ségalat, L. Genetic evidence for a
1084 dystrophin-glycoprotein complex (DGC) in Caenorhabditis elegans. *Gene* **294**, 77–86 (2002).

1085 45. Johnson, R. P., Kang, S. H. & Kramer, J. M. C. elegans dystroglycan DGN-1 functions in
1086 epithelia and neurons, but not muscle, and independently of dystrophin. *Development* **133**,
1087 1911–1921 (2006).

1088 46. Talts, J. F., Andac, Z., Göhring, W., Brancaccio, A. & Timpl, R. Binding of the G domains
1089 of laminin α1 and α2 chains and perlecan to heparin, sulfatides, α-dystroglycan and several
1090 extracellular matrix proteins. *Embo J* **18**, 863–870 (1999).

1091 47. Ishikawa-Sakurai, M., Yoshida, M., Imamura, M., Davies, K. E. & Ozawa, E. ZZ domain is
1092 essentially required for the physiological binding of dystrophin and utrophin to β-
1093 dystroglycan. *Hum Mol Genet* **13**, 693–702 (2004).

1094 48. Bunnell, T. M., Jaeger, M. A., Fitzsimons, D. P., Prins, K. W. & Ervasti, J. M.
1095 Destabilization of the Dystrophin-Glycoprotein Complex without Functional Deficits in α-
1096 Dystrobrevin Null Muscle. *PLoS ONE* **3**, e2604 (2008).

1097 49. Keeley, D. P. *et al.* Comprehensive Endogenous Tagging of Basement Membrane
1098 Components Reveals Dynamic Movement within the Matrix Scaffolding. *Dev Cell* **54**, 60-
1099 74.e7 (2020).

1100 50. Holt, K. H. & Campbell, K. P. Assembly of the Sarcoglycan Complex INSIGHTS FOR
1101 MUSCULAR DYSTROPHY*. *J Biol Chem* **273**, 34667–34670 (1998).

1102 51. Mlodzik, M. Chapter Five The Dishevelled Protein Family Still Rather a Mystery After
1103 Over 20 Years of Molecular Studies. *Curr Top Dev Biol* **117**, 75–91 (2016).

1104 52. Zhou, X. *et al.* The HSPG syndecan is a core organizer of cholinergic synapses. *J Cell*
1105 *Biology* **220**, e202011144 (2021).

1106 53. Song, S. *et al.* A Wnt-Frz/Ror-Dsh Pathway Regulates Neurite Outgrowth in
1107 Caenorhabditis elegans. *Plos Genet* **6**, e1001056 (2010).

1108 54. Jensen, M. *et al.* Wnt Signaling Regulates Acetylcholine Receptor Translocation and
1109 Synaptic Plasticity in the Adult Nervous System. *Cell* **149**, 173–187 (2012).

1110 55. Yamamoto, Y., Takeshita, H. & Sawa, H. Multiple Wnts Redundantly Control Polarity
1111 Orientation in Caenorhabditis elegans Epithelial Stem Cells. *PLoS Genet.* **7**, e1002308
1112 (2011).

1113 56. Ho, H.-Y. H. *et al.* Wnt5a–Ror–Dishevelled signaling constitutes a core developmental
1114 pathway that controls tissue morphogenesis. *Proc. Natl. Acad. Sci.* **109**, 4044–4051 (2012).

1115 57. Susman, M. W. *et al.* Kinesin superfamily protein Kif26b links Wnt5a-Ror signaling to the
1116 control of cell and tissue behaviors in vertebrates. *eLife* **6**, e26509 (2017).

1117 58. Guillabert-Gourgues, A. *et al.* Kif26b controls endothelial cell polarity through the
1118 Dishevelled/Daam1-dependent planar cell polarity–signaling pathway. *Mol. Biol. Cell* **27**,
1119 941–953 (2016).

1120 59. Sewduth, R. N. *et al.* The ubiquitin ligase PDZRN3 is required for vascular
1121 morphogenesis through Wnt/planar cell polarity signalling. *Nat. Commun.* **5**, 4832 (2014).

1122 60. Konopelski Snavely, S. E. *et al.* Proteomic analysis identifies the E3 ubiquitin ligase
1123 Pdzrn3 as a regulatory target of Wnt5a-Ror signaling. *Proc. Natl. Acad. Sci.* **118**,
1124 e2104944118 (2021).

1125 61. Wang, J. *et al.* Regulation of polarized extension and planar cell polarity in the cochlea by
1126 the vertebrate PCP pathway. *Nat. Genet.* **37**, 980–985 (2005).

1127 62. Tree, D. R. P. *et al.* Prickle Mediates Feedback Amplification to Generate Asymmetric
1128 Planar Cell Polarity Signaling. *Cell* **109**, 371–381 (2002).

1129 63. Wang, J. & Ding, M. Robo and Ror function in a common receptor complex to regulate
1130 Wnt-mediated neurite outgrowth in Caenorhabditis elegans. *Proc National Acad Sci* **115**,
1131 201717468 (2018).

1132 64. Zheng, C., Diaz-Cuadros, M. & Chalfie, M. Dishevelled attenuates the repelling activity of
1133 Wnt signaling during neurite outgrowth in Caenorhabditis elegans. *Proc National Acad Sci*
1134 **112**, 13243–13248 (2015).

1135 65. Gao, B. *et al.* Wnt Signaling Gradients Establish Planar Cell Polarity by Inducing Vangl2
1136 Phosphorylation through Ror2. *Dev. Cell* **20**, 163–176 (2011).

1137 66. Petkova, M. V. *et al.* Characterization of a DmdEGFP reporter mouse as a tool to
1138 investigate dystrophin expression. *Skelet Muscle* **6**, 25 (2016).

1139 67. Petkova, M. V. *et al.* Live-imaging of revertant and therapeutically restored dystrophin in
1140 the DmdEGFP-mdx mouse model for Duchenne muscular dystrophy. *Neuropath Appl Neuro*
1141 **46**, 602–614 (2020).

1142 68. Morin, A. *et al.* Dystrophin myonuclear domain restoration governs treatment efficacy in
1143 dystrophic muscle. *Proc National Acad Sci* **120**, e2206324120 (2023).

1144 69. Ruf-Zamojski, F., Trivedi, V., Fraser, S. E. & Trinh, L. A. Spatio-Temporal Differences in
1145 Dystrophin Dynamics at mRNA and Protein Levels Revealed by a Novel FlipTrap Line. *Plos*
1146 *One* **10**, e0128944 (2015).

1147 70. Dumont, N. A. *et al.* Dystrophin expression in muscle stem cells regulates their polarity
1148 and asymmetric division. *Nat Med* **21**, 1455–1463 (2015).

1149 71. Dennis, C., Pouchin, P., Richard, G. & Mirouse, V. Basement membrane diversification
1150 relies on two competitive secretory routes defined by Rab10 and Rab8 and modulated by
1151 dystrophin and the exocyst complex. *bioRxiv* 2023.03.22.533752 (2023)
1152 doi:10.1101/2023.03.22.533752.

1153 72. Campos, F. C. *et al.* Oriented basement membrane fibrils provide a memory for F-actin
1154 planar polarization via the Dystrophin-Dystroglycan complex during tissue elongation.
1155 *Development* **147**, dev186957 (2020).

1156 73. Belhasan, D. C. & Akaaboune, M. The role of the Dystrophin Glycoprotein Complex on
1157 the Neuromuscular System. *Neurosci Lett* **722**, 134833 (2020).

1158 74. Constantin, B. Dystrophin complex functions as a scaffold for signalling proteins.
1159 *Biochimica Et Biophysica Acta Bba - Biomembr* **1838**, 635–642 (2014).

1160 75. Brouilly, N. *et al.* Ultra-structural time-course study in the C. elegans model for Duchenne
1161 muscular dystrophy highlights a crucial role for sarcomere-anchoring structures and
1162 sarcolemma integrity in the earliest steps of the muscle degeneration process. *Hum Mol*
1163 *Genet* **24**, 6428–6445 (2015).

1164 76. Brenner, S. The genetics of Caenorhabditis elegans. *Genetics* **77**, 71–94 (1974).

1165 77. Postma, M. & Goedhart, J. PlotsOfData-A web app for visualizing data together with their
1166 summaries. *PLoS Biology* **17**, e3000202 (2019).

1167

1168

1169 **Supplementary Table S6: Conservation of DAPC components in vertebrates**
1170 **and *C. elegans***

1171

Vertebrates	***C. elegans***
Dystrophin, Utrophin, DRP2	DYS-1
Dystroglycan (DAG1)	DGN-1
Dystrobrevin α,β	DYB-1
Syntrophin-α1,-β1,-β2	STN-1
Syntrophin -γ1,-γ2	STN-2
Sarcoglycan-α,-ε	SGCA-1
Sarcoglycan-β	SGCB-1
Sarcoglycan-δ,-γ	SGN-1

1172

Figure 1

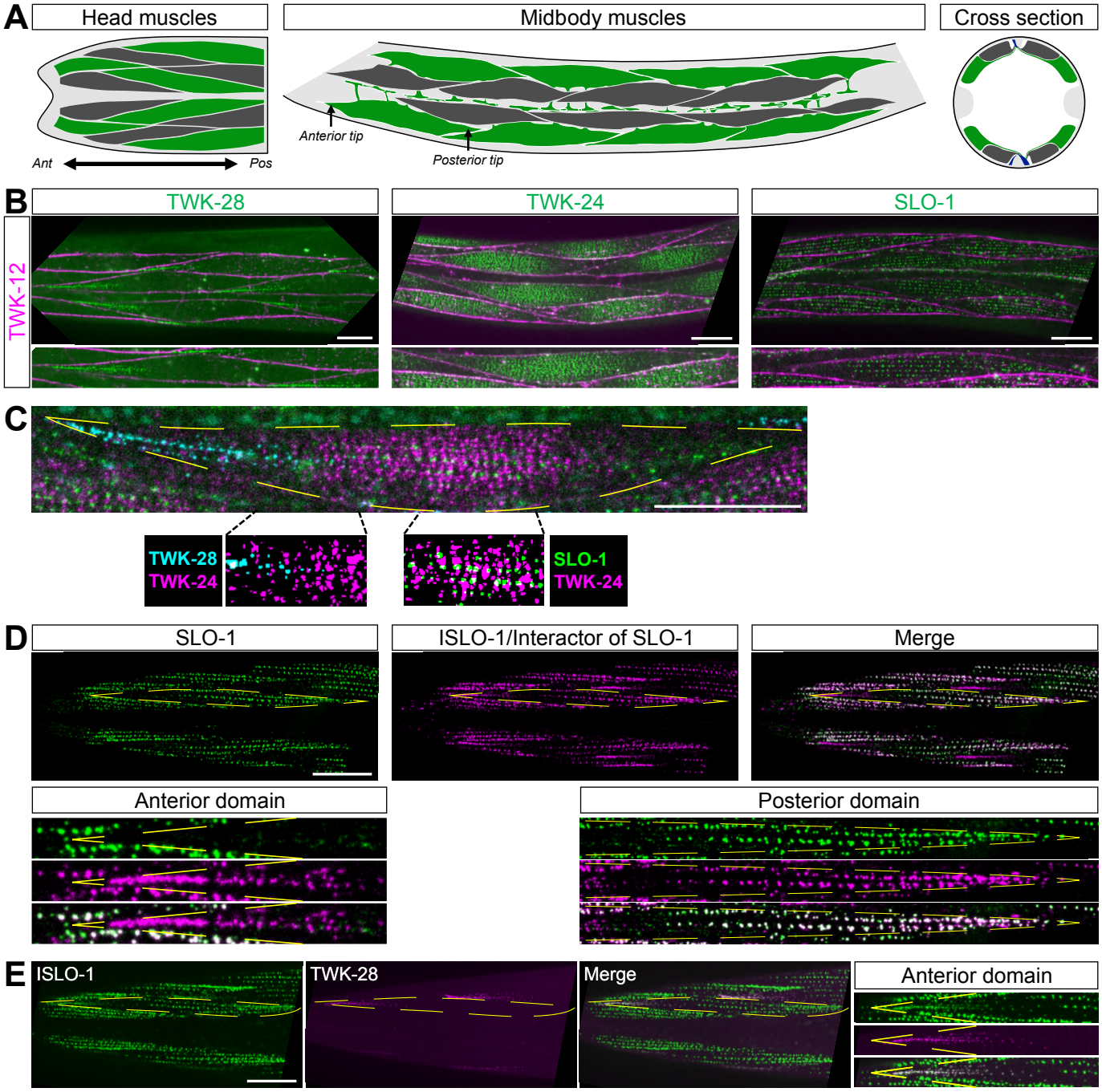
A
Head muscles
Midbody muscles
Cross section
Ant
Pos
Anterior tip
Posterior tip
B
TWK-28
TWK-24
SLO-1
TWK-12
C
TWK-28
TWK-24
SLO-1
TWK-24
D
SLO-1
ISLO-1/Interactor of SLO-1
Merge
Anterior domain
Posterior domain
E
ISLO-1
TWK-28
Merge
Anterior domain

Figure 2

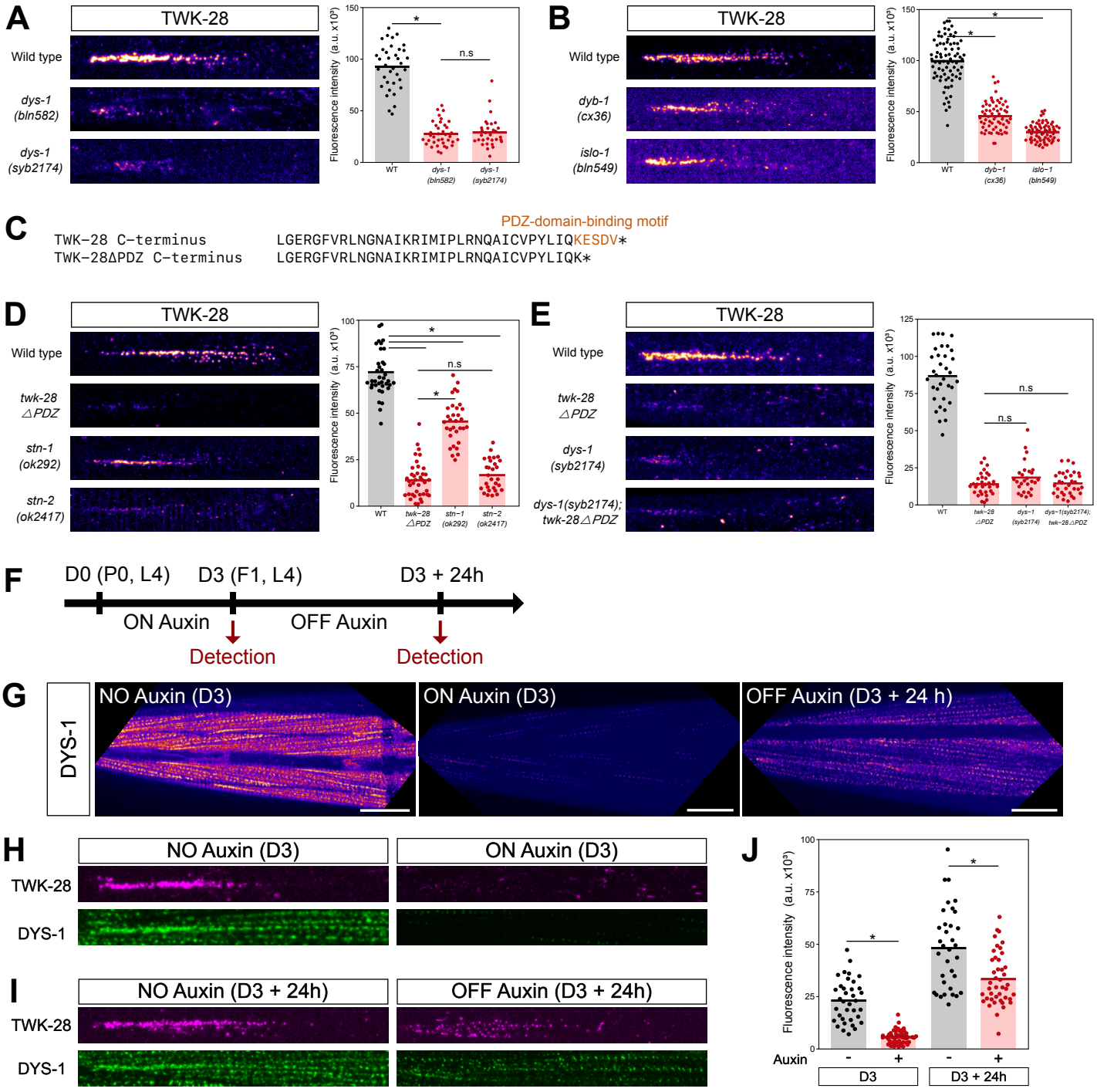
A
TWK-28
Wild type
dys-1 (bln582)
dys-1 (syb2174)
Fluorescence intensity (a.u. x10³)
*
n.s
WT
dys-1 (bln582)
dys-1 (syb2174)
B
TWK-28
Wild type
dyb-1 (cx36)
islo-1 (bln549)
Fluorescence intensity (a.u. x10³)
*
*
WT
dyb-1 (cx36)
islo-1 (bln549)
C
PDZ-domain-binding motif
TWK-28 C-terminus LGERGFVRLNGNAIKRIMIPLRNQAICVPYLIQKESDV*
TWK-28ΔPDZ C-terminus LGERGFVRLNGNAIKRIMIPLRNQAICVPYLIQK*
D
TWK-28
Wild type
twk-28 △PDZ
stn-1 (ok292)
stn-2 (ok2417)
Fluorescence intensity (a.u. x10³)
*
n.s
*
WT
twk-28 △PDZ
stn-1 (ok292)
stn-2 (ok2417)
E
TWK-28
Wild type
twk-28 △PDZ
dys-1 (syb2174)
dys-1(syb2174); twk-28△PDZ
Fluorescence intensity (a.u. x10³)
n.s
n.s
WT
twk-28 △PDZ
dys-1 (syb2174)
dys-1(syb2174); twk-28△PDZ
F
D0 (P0, L4)
D3 (F1, L4)
D3 + 24h
ON Auxin
OFF Auxin
Detection
Detection
G
DYS-1
NO Auxin (D3)
ON Auxin (D3)
OFF Auxin (D3 + 24 h)
H
NO Auxin (D3)
ON Auxin (D3)
TWK-28
DYS-1
I
NO Auxin (D3 + 24h)
OFF Auxin (D3 + 24h)
TWK-28
DYS-1
J
Fluorescence intensity (a.u. x10³)
*
*
Auxin
-
+
-
+
D3
D3 + 24h

Figure 3

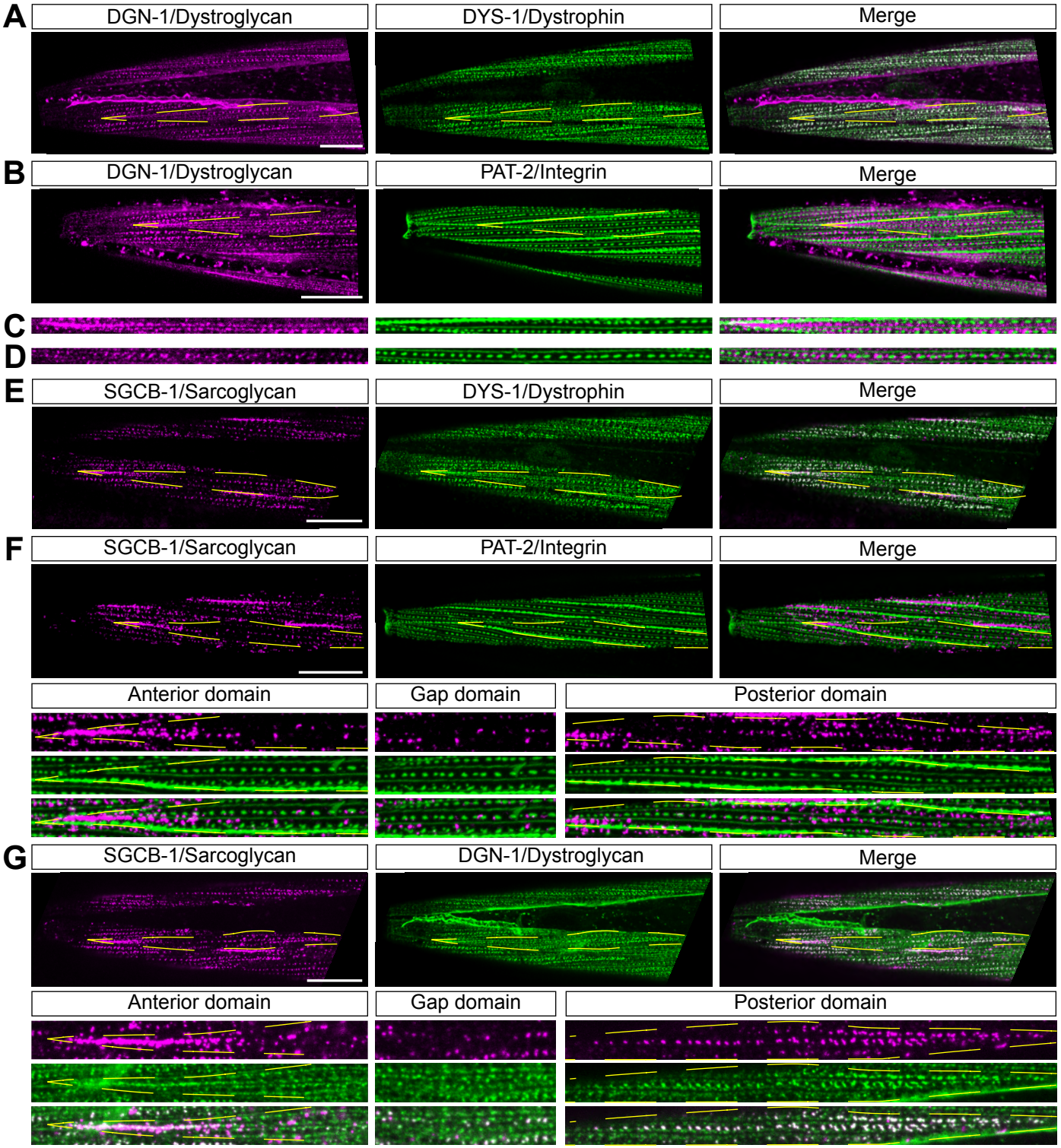
A
DGN-1/Dystroglycan
DYS-1/Dystrophin
Merge
B
DGN-1/Dystroglycan
PAT-2/Integrin
Merge
C
D
E
SGCB-1/Sarcoglycan
DYS-1/Dystrophin
Merge
F
SGCB-1/Sarcoglycan
PAT-2/Integrin
Merge
Anterior domain
Gap domain
Posterior domain
G
SGCB-1/Sarcoglycan
DGN-1/Dystroglycan
Merge
Anterior domain
Gap domain
Posterior domain

Figure 4

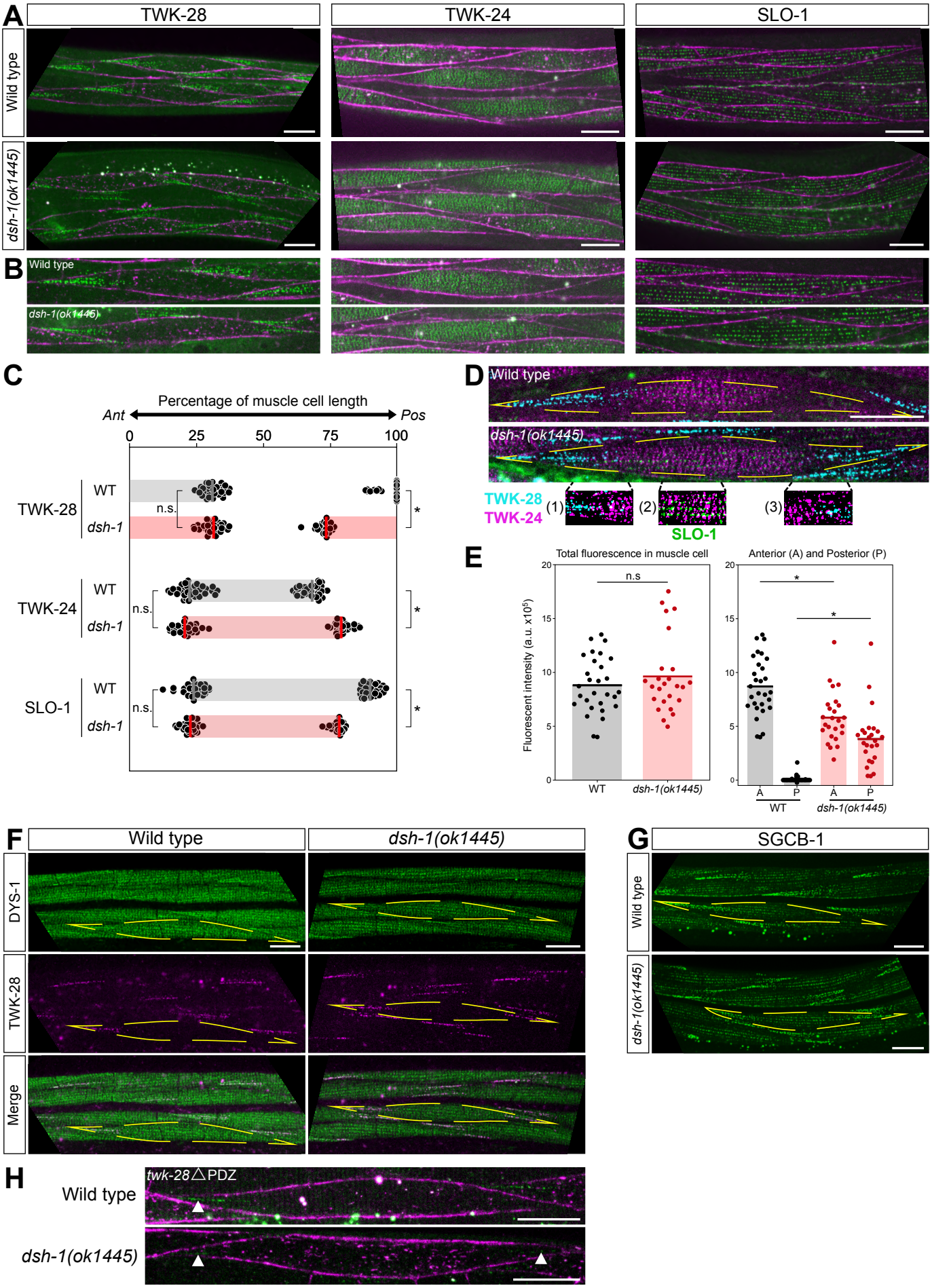
A
TWK-28
TWK-24
SLO-1
Wild type
dsh-1(ok1445)
B
Wild type
dsh-1(ok1445)
C
Percentage of muscle cell length
Ant
Pos
0
25
50
75
100
TWK-28
TWK-24
SLO-1
WT
dsh-1
n.s.
*
D
Wild type
dsh-1(ok1445)
TWK-28
TWK-24
SLO-1
(1)
(2)
(3)
E
Total fluorescence in muscle cell
Anterior (A) and Posterior (P)
Fluorescent intensity (a.u. x10^5)
n.s
*
WT
dsh-1(ok1445)
A
P
F
Wild type
dsh-1(ok1445)
DYS-1
TWK-28
Merge
G
SGCB-1
Wild type
dsh-1(ok1445)
H
Wild type
dsh-1(ok1445)
twk-28△PDZ

Figure 5

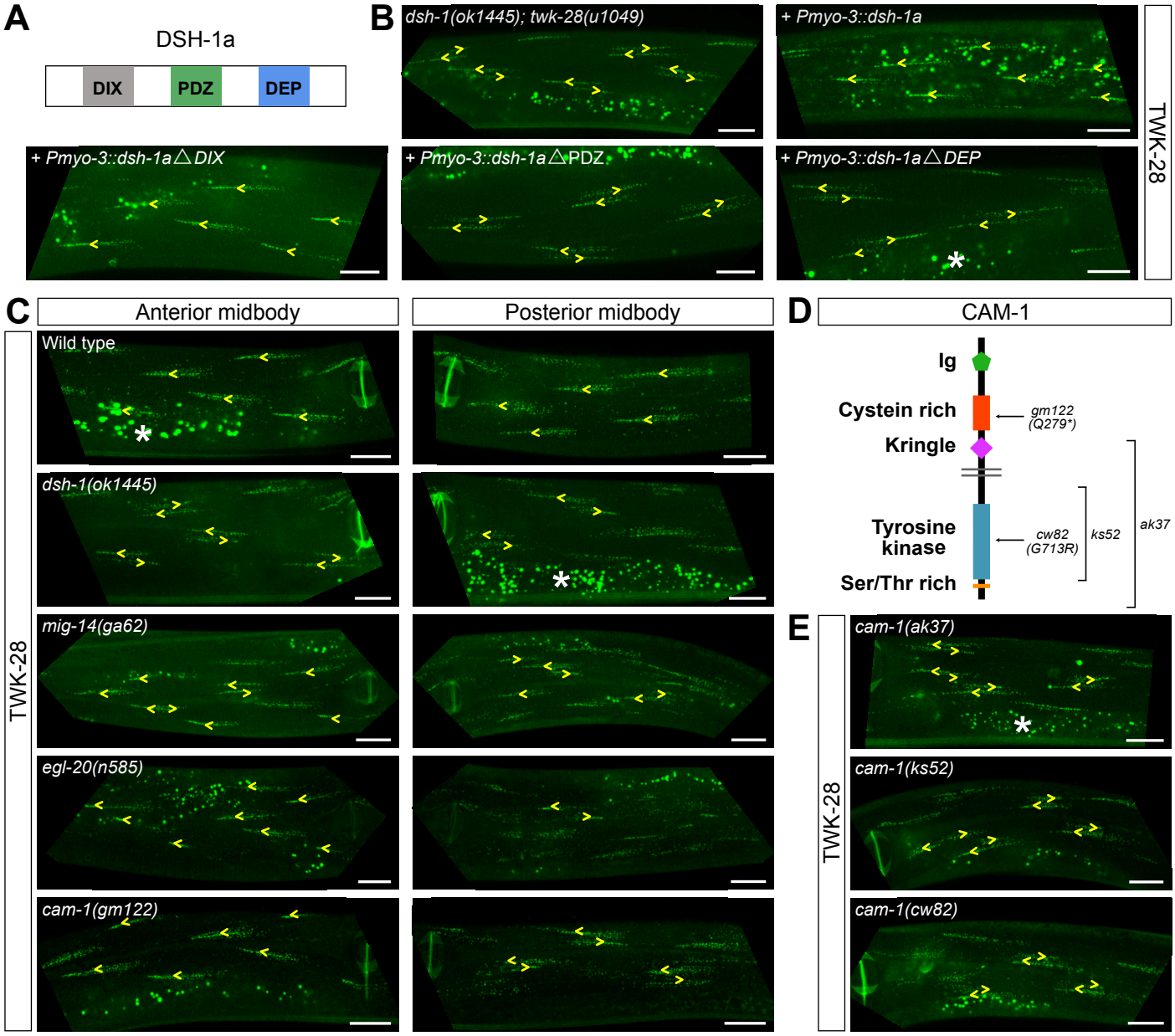
A
DSH-1a
DIX
PDZ
DEP
B
dsh-1(ok1445); twk-28(u1049)
+ Pmyo-3::dsh-1a
+ Pmyo-3::dsh-1a△DIX
+ Pmyo-3::dsh-1a△PDZ
+ Pmyo-3::dsh-1a△DEP
TWK-28
C
Anterior midbody
Posterior midbody
TWK-28
Wild type
dsh-1(ok1445)
mig-14(ga62)
egl-20(n585)
cam-1(gm122)
D
CAM-1
Ig
Cystein rich
Kringle
Tyrosine kinase
Ser/Thr rich
gm122 (Q279*)
cw82 (G713R)
ks52
ak37
E
TWK-28
cam-1(ak37)
cam-1(ks52)
cam-1(cw82)

Figure 6

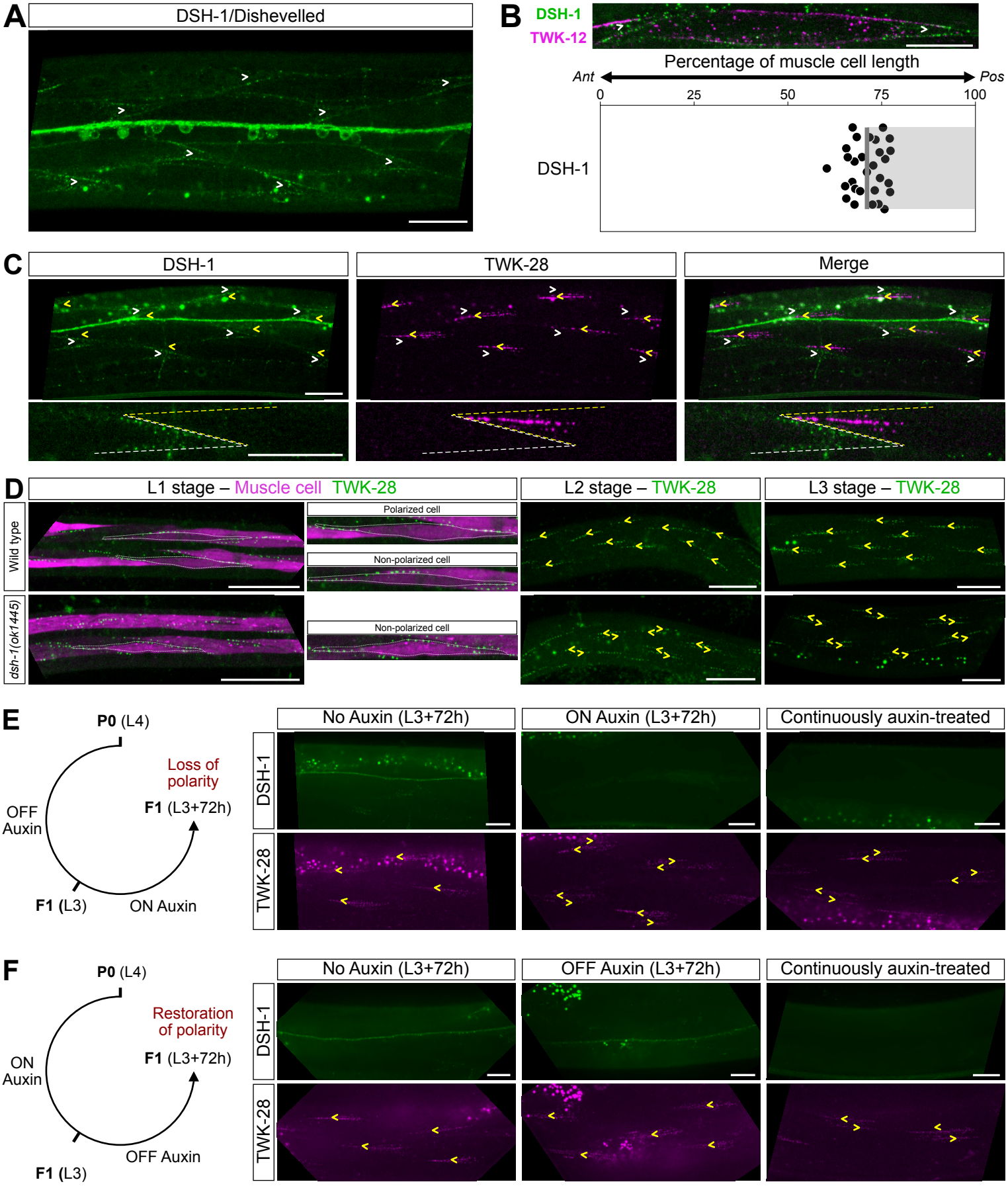
A
DSH-1/Dishevelled
B
DSH-1
TWK-12
Percentage of muscle cell length
Ant
Pos
0
25
50
75
100
DSH-1
C
DSH-1
TWK-28
Merge
D
L1 stage – Muscle cell TWK-28
L2 stage – TWK-28
L3 stage – TWK-28
Wild type
dsh-1(ok1445)
Polarized cell
Non-polarized cell
Non-polarized cell
E
P0 (L4)
Loss of polarity
F1 (L3+72h)
OFF Auxin
F1 (L3)
ON Auxin
No Auxin (L3+72h)
ON Auxin (L3+72h)
Continuously auxin-treated
DSH-1
TWK-28
F
P0 (L4)
Restoration of polarity
F1 (L3+72h)
ON Auxin
OFF Auxin
F1 (L3)
No Auxin (L3+72h)
OFF Auxin (L3+72h)
Continuously auxin-treated
DSH-1
TWK-28

Figure S1

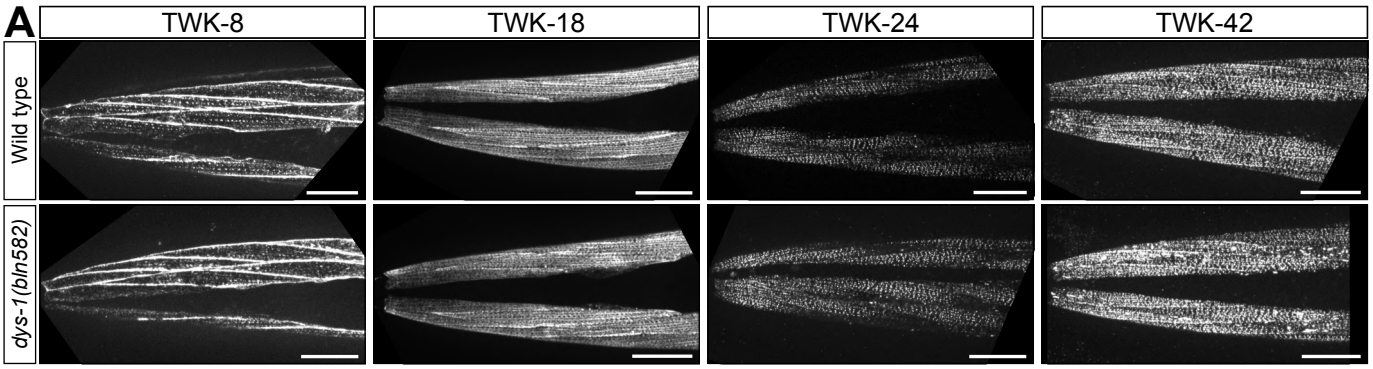

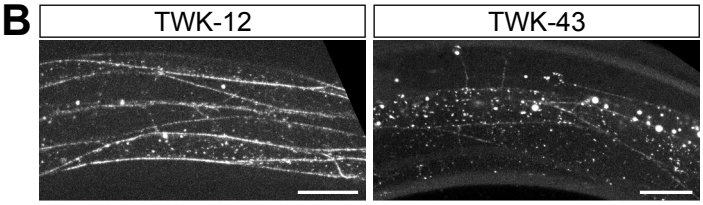

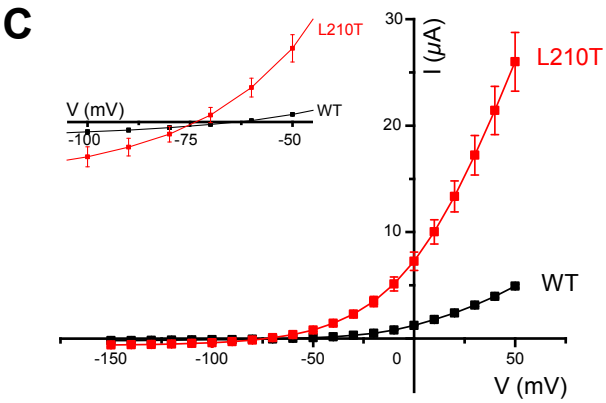

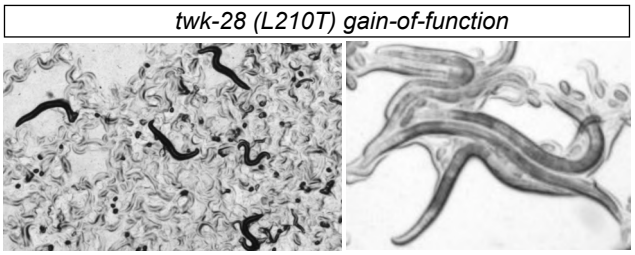

E

Allele	Locus	Mutation	Effect
bln557	*dys-1*	G to A ; ChrI:11556770	Q30Ochre
bln545	*dys-1*	C to T ; ChrI:11556616	W81Amber
bln582	*dys-1*	C to T ; ChrI:11556528	W110Opal
bln554	*dys-1*	C to T ; ChrI:11556280	W138Amber
bln583	*dys-1*	T to A ; ChrI:11544157	K1527Amber
bln568	*dys-1*	G to A ; ChrI:11543893	Q1615Ochre
bln552	*dys-1*	C to T ; ChrI:11540064	W2277Opal
bln571	*dys-1*	C to A ; ChrI:11538895	E2442Ochre
bln565	*dys-1*	C to T ; ChrI:11538087	W2582Opal
bln573	*dys-1*	G to A ; ChrI:11537052	Q2695Ochre
bln566	*dys-1*	C to T ; ChrI:11536816	W2773Opal
bln564	*dys-1*	C to T ; ChrI:11536387	W2807Amber
bln562	*dys-1*	G to A ; ChrI:11534654	Q2992Ochre
bln556	*dys-1*	G to A ; ChrI:11532291	loss of splice-donor
bln549	*islo-1*	G to A ; ChrIV:8137939	G165D

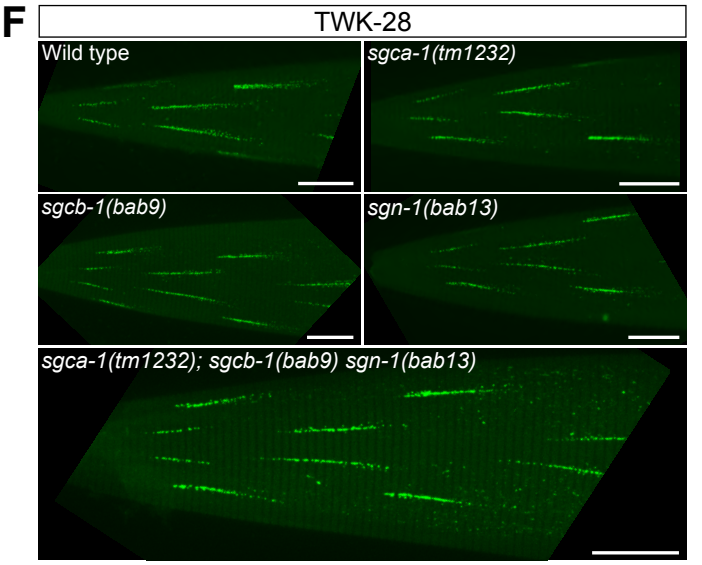

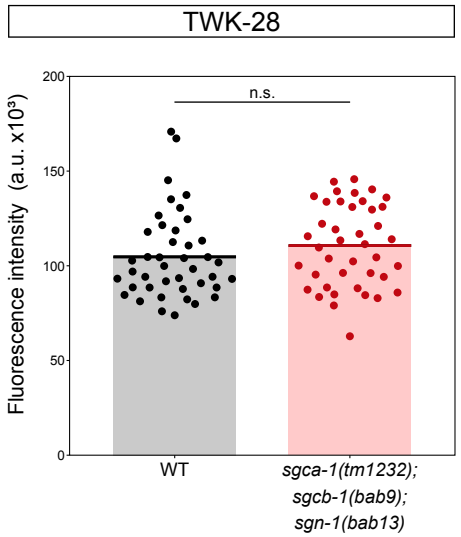

Figure S2

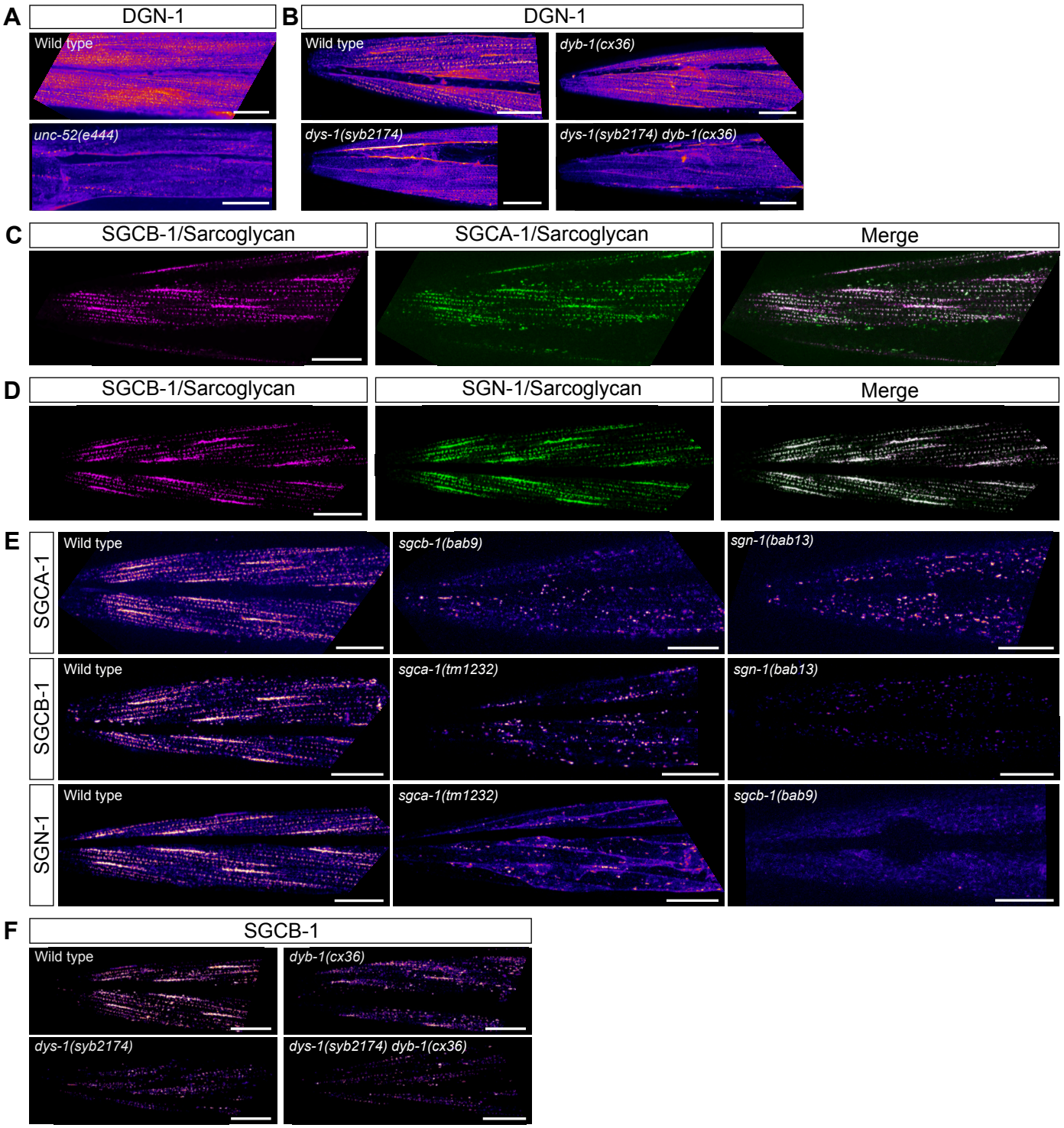
A
DGN-1
Wild type
unc-52(e444)
B
DGN-1
Wild type
dyb-1(cx36)
dys-1(syb2174)
dys-1(syb2174) dyb-1(cx36)
C
SGCB-1/Sarcoglycan
SGCA-1/Sarcoglycan
Merge
D
SGCB-1/Sarcoglycan
SGN-1/Sarcoglycan
Merge
E
SGCA-1
Wild type
sgcb-1(bab9)
sgn-1(bab13)
SGCB-1
Wild type
sgca-1(tm1232)
sgn-1(bab13)
SGN-1
Wild type
sgca-1(tm1232)
sgcb-1(bab9)
F
SGCB-1
Wild type
dyb-1(cx36)
dys-1(syb2174)
dys-1(syb2174) dyb-1(cx36)

Figure S3

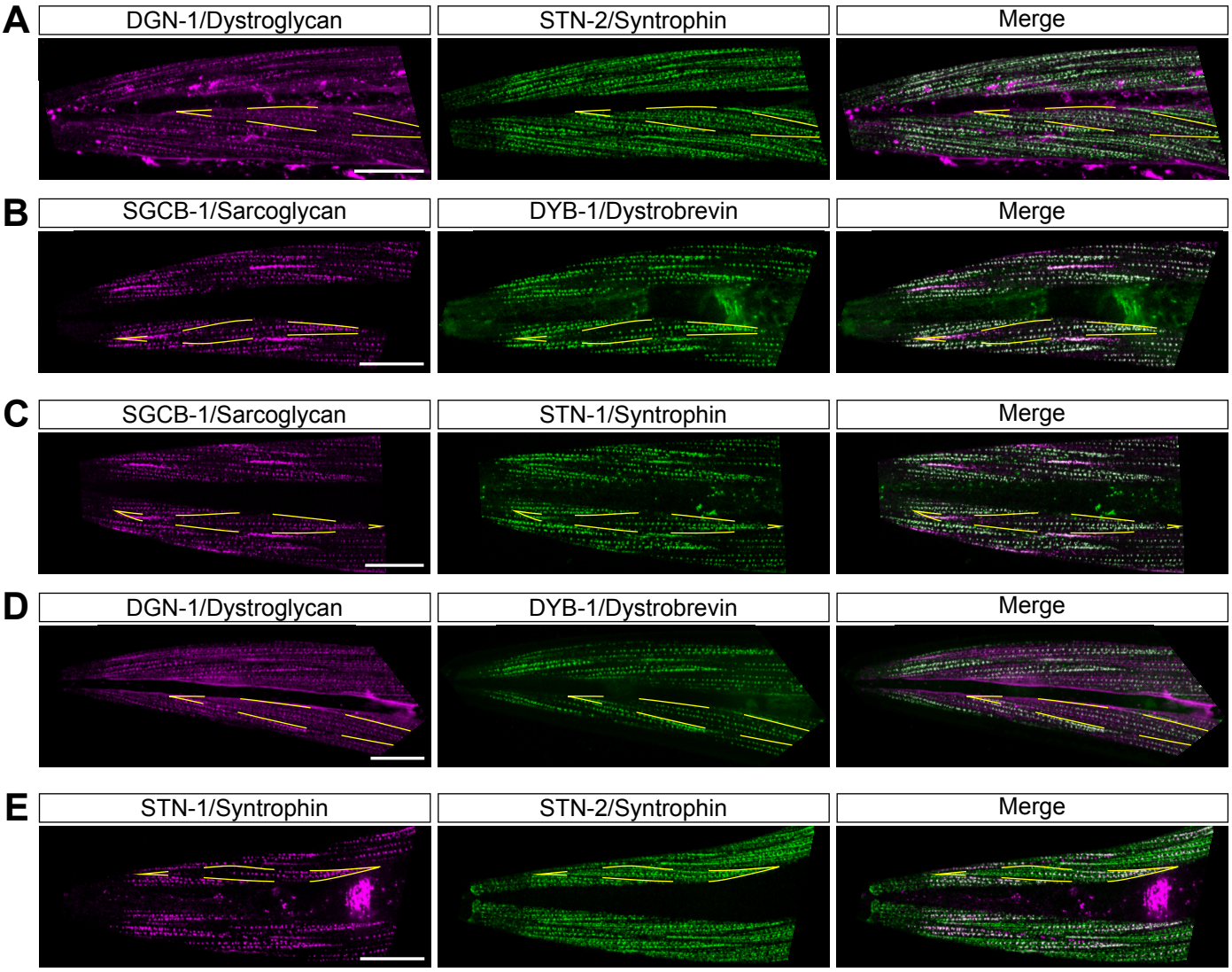
A
DGN-1/Dystroglycan
STN-2/Syntrophin
Merge
B
SGCB-1/Sarcoglycan
DYB-1/Dystrobrevin
Merge
C
SGCB-1/Sarcoglycan
STN-1/Syntrophin
Merge
D
DGN-1/Dystroglycan
DYB-1/Dystrobrevin
Merge
E
STN-1/Syntrophin
STN-2/Syntrophin
Merge

Figure S4

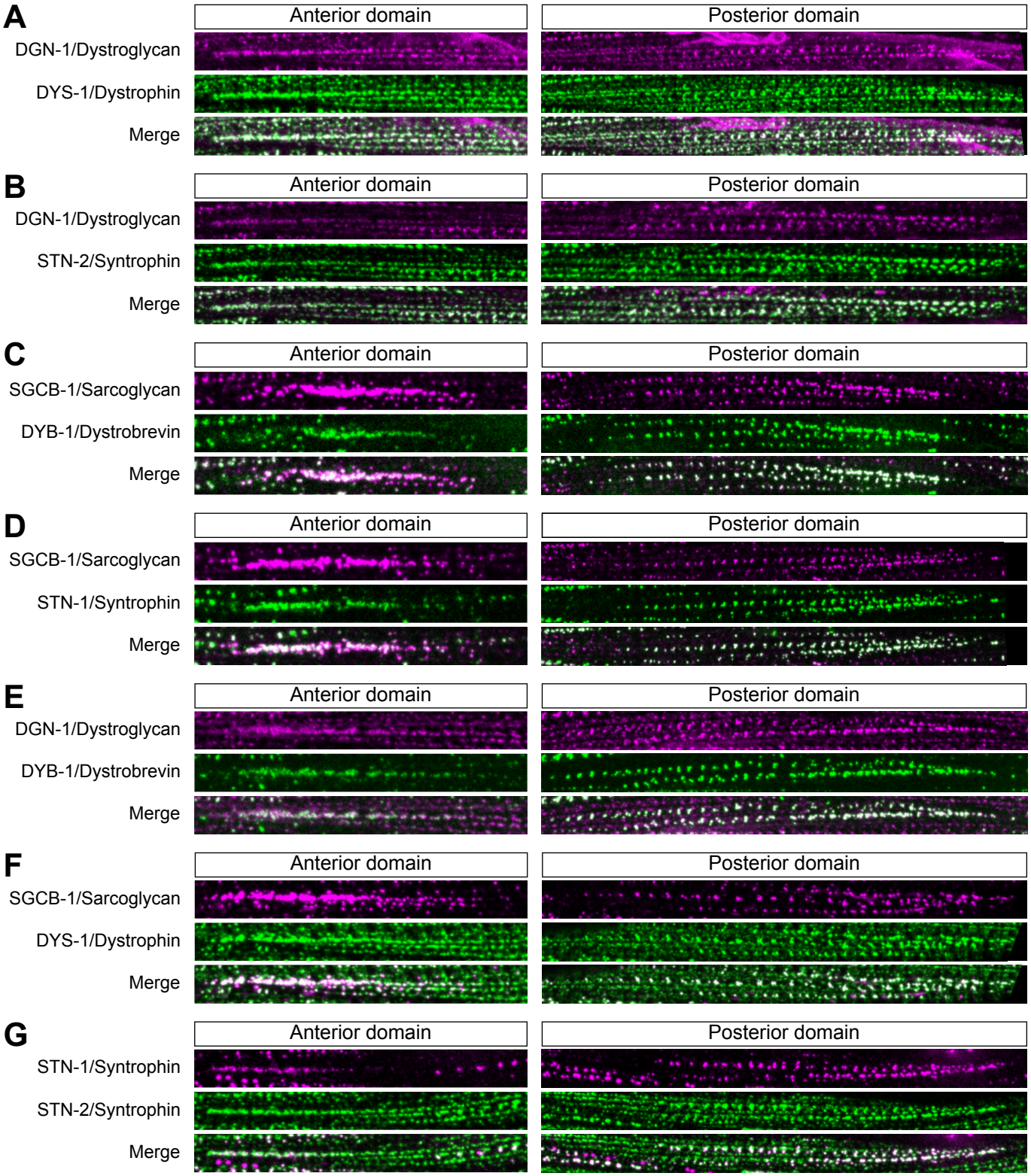
A
Anterior domain
Posterior domain
DGN-1/Dystroglycan
DYS-1/Dystrophin
Merge
B
Anterior domain
Posterior domain
DGN-1/Dystroglycan
STN-2/Syntrophin
Merge
C
Anterior domain
Posterior domain
SGCB-1/Sarcoglycan
DYB-1/Dystrobrevin
Merge
D
Anterior domain
Posterior domain
SGCB-1/Sarcoglycan
STN-1/Syntrophin
Merge
E
Anterior domain
Posterior domain
DGN-1/Dystroglycan
DYB-1/Dystrobrevin
Merge
F
Anterior domain
Posterior domain
SGCB-1/Sarcoglycan
DYS-1/Dystrophin
Merge
G
Anterior domain
Posterior domain
STN-1/Syntrophin
STN-2/Syntrophin
Merge

Figure S5

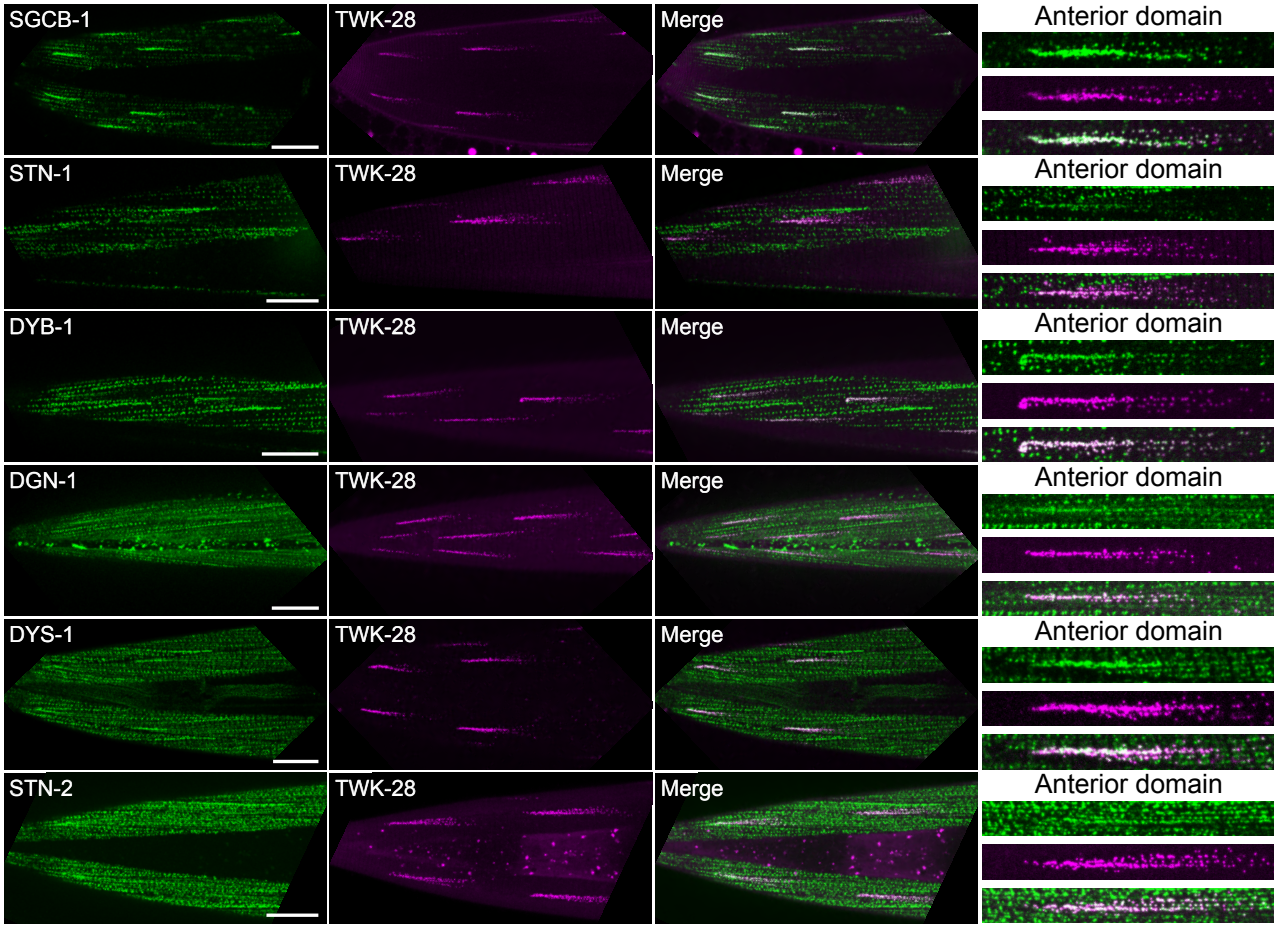
SGCB-1
TWK-28
Merge
Anterior domain
STN-1
TWK-28
Merge
Anterior domain
DYB-1
TWK-28
Merge
Anterior domain
DGN-1
TWK-28
Merge
Anterior domain
DYS-1
TWK-28
Merge
Anterior domain
STN-2
TWK-28
Merge
Anterior domain

Figure S6

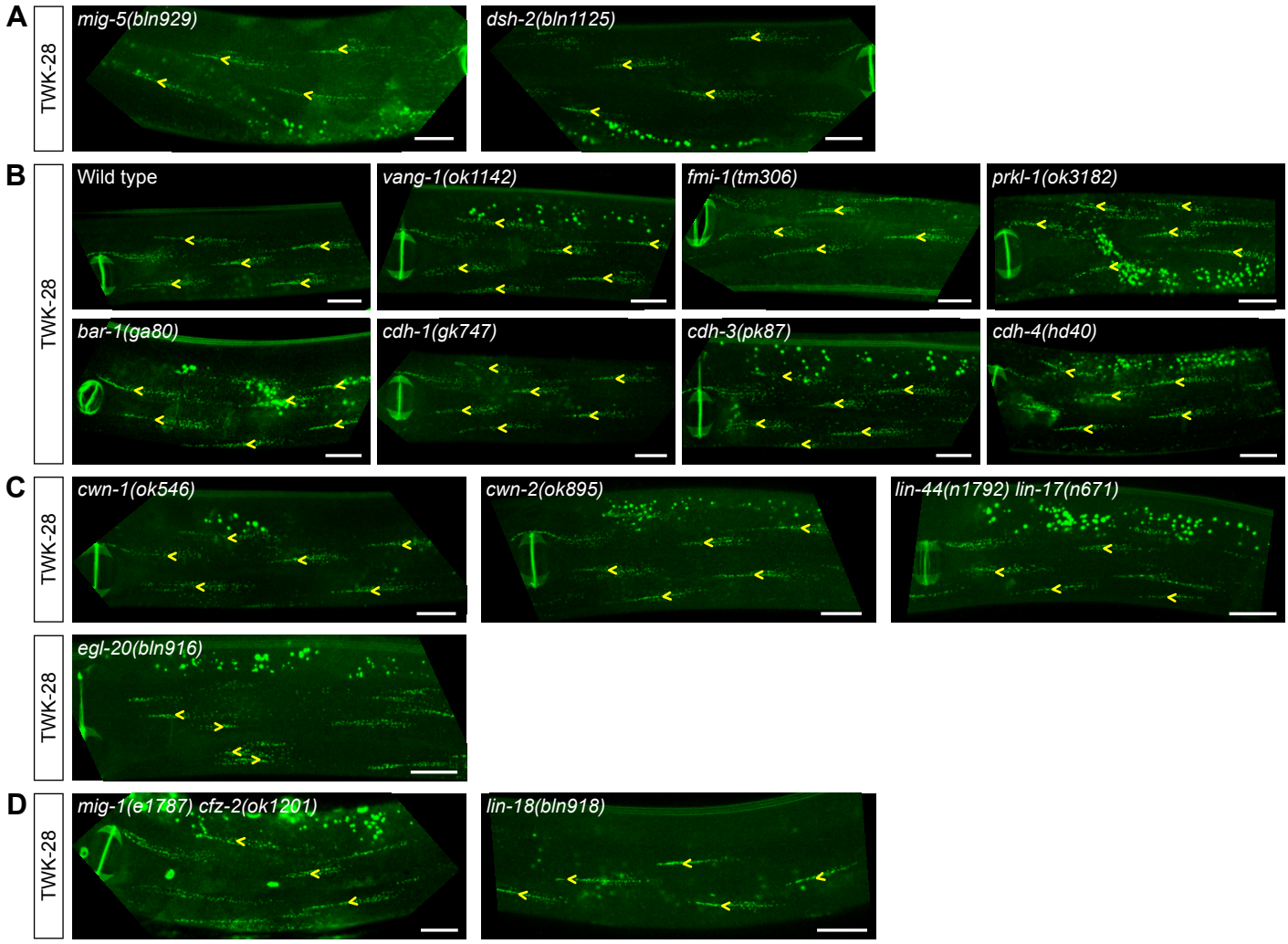
A
TWK-28
mig-5(bln929)
dsh-2(bln1125)
B
TWK-28
Wild type
vang-1(ok1142)
fmi-1(tm306)
prkl-1(ok3182)
bar-1(ga80)
cdh-1(gk747)
cdh-3(pk87)
cdh-4(hd40)
C
TWK-28
cwn-1(ok546)
cwn-2(ok895)
lin-44(n1792) lin-17(n671)
TWK-28
egl-20(bln916)
D
TWK-28
mig-1(e1787) cfz-2(ok1201)
lin-18(bln918)

Figure S7

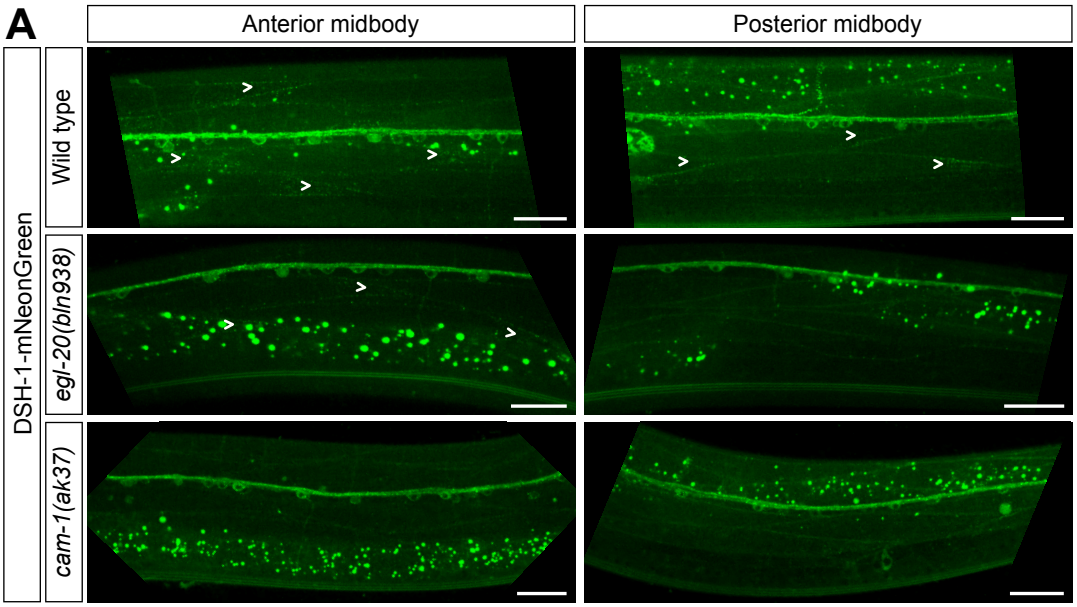
A
Anterior midbody
Posterior midbody
DSH-1-mNeonGreen
Wild type
egl-20(bln938)
cam-1(ak37)

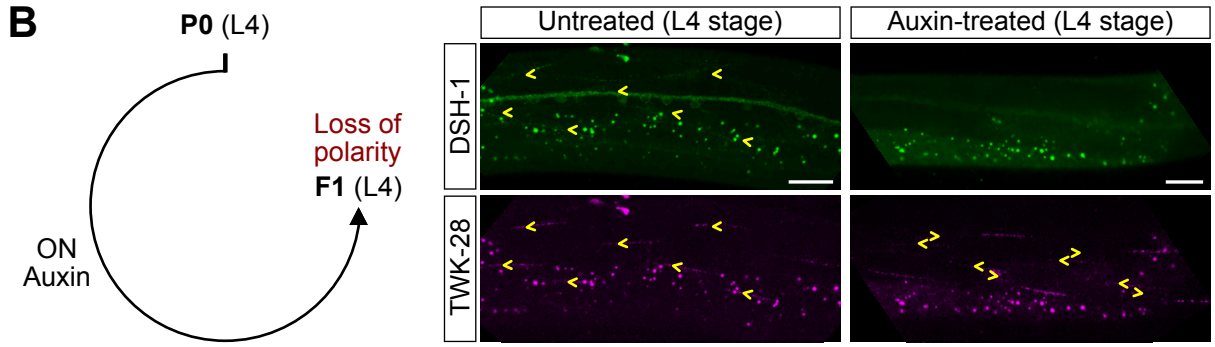
B
P0 (L4)
Loss of polarity
F1 (L4)
ON Auxin
Untreated (L4 stage)
Auxin-treated (L4 stage)
DSH-1
TWK-28